

A Systematic Analysis of Out-of-Distribution Detection Under Representation and Training Paradigm Shifts

Claudio César Claros-Olivares¹ Austin J. Brockmeier¹

Abstract

We present the largest systematic comparison to date of out-of-distribution (OOD) detection methods using AURC and AUGRC as primary metrics. Our comparison explores different regimes of distribution shift (stratified by CLIP embeddings of the out-of-distribution image datasets) with varying numbers of classes and uses a representation-centric view of OOD detection, including neural collapse metrics, for subsequent analysis. Together the empirical results and representation analysis provides novel insights and statistically grounded guidance for method selection under distribution shift. Experiments cover two representation paradigms: CNNs trained from scratch and a fine-tuned Vision Transformer (ViT), evaluated on CIFAR-10/100, SuperCIFAR-100, and TinyImageNet. Using a multiple-comparison-controlled, rank-based pipeline (Friedman test with Conover–Holm post-hoc) and Bron–Kerbosch cliques, we find that the learned feature space largely determines OOD efficacy. For both CNNs and ViTs, probabilistic scores (e.g., MSR, GEN) dominate misclassification (ID) detection. Under stronger shifts, geometry-aware scores (e.g., NNGuide, fDBD, CTM) prevail on CNNs, whereas on ViTs Grad-Norm and KPCA Reconstruction Error remain consistently competitive. We further show a class-count-dependent trade-off for Monte-Carlo Dropout (MCD) and that a simple PCA projection improves several detectors. The neural-collapse-based geometric analysis explains when prototype and boundary-based scores become optimal under strong shifts.

1. Introduction

In recent years, there has been a significant increase in approaches dealing with out-of-distribution (OOD) detection (Ammar et al., 2023; Bibas et al., 2021; Hendrycks & Gimpel, 2016; Hendrycks et al., 2019; Huang et al., 2021; Lee et al., 2018; Liu & Qin, 2023; Liu et al., 2020; 2023; Ngoc-Hieu et al., 2023; Park et al., 2023; Wang et al., 2022) given their relevance in the reliable deployment of deep learning models, particularly in safety-critical applications. A significant vulnerability of deep neural networks (DNNs) is their tendency to produce *silent failures* (Jaeger et al., 2022; Traub et al., 2024), which are conceptualized as incorrect predictions with high confidence that are hard to detect. A reliable DNN classifier should not only accurately classify known in-distribution (ID) samples, but also effectively flag OOD inputs as *unknown*. However, many OOD detection methods have inconsistent behavior across datasets. For instance, the widely used maximum softmax response (MSR) (Hendrycks & Gimpel, 2016), a strong baseline for small-scale OOD detection, does not scale well to challenging conditions presented by large datasets such as ImageNet-1k (Deng et al., 2009). Hendrycks et al. (2019) hypothesizes that in datasets with many visually similar classes, a classifier might produce low softmax confidence for a legitimate ID image not due to unfamiliarity, but because the precise class is difficult to determine, dispersing the probability mass. This issue makes MSR problematic for large-scale detection. In contrast, the maximum logit score (MLS) (Hendrycks et al., 2019), which uses the negative of the maximum unnormalized logit, was proposed as a better baseline for large-scale OOD detection. Experiments showed that MLS significantly outperforms MSR in large-scale datasets, with improvements over 10% AUROC in some cases, whereas the difference was minor on small-scale CIFAR-10. This highlights the inconsistencies in performance as the number of training classes increases.

Furthermore, some methods that performed well in small-scale settings, such as the Mahalanobis distance (Lee et al., 2018), encountered numerical problems when scaled to 1000 classes (Hendrycks et al., 2019). Mahalanobis distance utilizes a mixture of class-conditional Gaussians on features to identify OOD samples, showing effectiveness

¹Department of Electrical & Computer Engineering, University of Delaware, Delaware, USA. Correspondence to: Claudio César Claros-Olivares <cesar@udel.edu>, Austin J. Brockmeier <ajb@udel.edu>.

on datasets like CIFAR-10. However, its scaling issues underscore that methods that rely on specific feature space properties derived from training data can become unstable or computationally challenging with a large number of classes. In addition, the observation that methods that are effective in natural images might differ from those for other data types, such as medical images (Gutbrod et al., 2025), where feature-based methods might excel, also subtly suggests that data scale and complexity, often correlated with the number of classes, influence the effectiveness of the method.

By contrasting multiple OOD detection methods and performance metrics obtained using CIFAR-10, CIFAR-100 (including superclasses) and TinyImagenet as ID datasets evaluated in near, mid and far OOD scenarios, we highlight the varying effectiveness of methods across different scales and the need for approaches specifically designed or validated depending on the number of classes in the training set. The four main contributions of our work are **1**) a representation- and training-aware experimental design that factorially varies the backbone (CNN vs ViT), the training paradigm, and the confidence scoring function (CSF); **2**) a statistically rigorous comparison using AURC/AUGRC, non-parametric tests, and clique-based equivalence classes; **3**) a CLIP-based stratification of OOD datasets into near/mid/far semantic regimes; and **4**) a neural-collapse-based theoretical analysis that explains when and why probabilistic vs geometry-aware vs gradient-based detectors dominate.¹

2. Related Work

The inconsistencies in OOD evaluation have spurred multiple benchmarking efforts to standardize procedures and report more comprehensive results. However, in general, the impact of the number of classes in the training set has been overlooked. Yang et al. (2022), for example, presents an extensive and unified benchmark framework designed to evaluate and compare out-of-distribution (OOD) detection methods across neighboring fields, including anomaly detection (AD), open set recognition (OSR), and model uncertainty estimation. Furthermore, the authors implement a codebase named *OpenOOD*, which integrates multiple OOD detection methods and evaluates them in a generalized OOD detection framework using 9 designed benchmarks and 4 OOD detection datasets that include MNIST, CIFAR-10, CIFAR-100, and ImageNet. Each benchmark features near-OOD (semantic shifts) and far-OOD (domain shifts) scenarios and reports AUROC, FPR@95, and AUPR as metrics. Specifically, they show that the best performing OOD detection methods between CIFAR-10 and CIFAR-100, considering near- and far-OOD scenarios, are not the

same. Also, the authors state that despite ImageNet’s higher complexity, ImageNet-based benchmarks sometimes yield higher OOD detection performance than CIFAR-10/100. In a follow-up work, Zhang et al. (2023) extended *OpenOOD*’s codebase, implementing more OOD detection methods and extending its evaluation capabilities to larger datasets and recent foundation models. Although both studies experiment with multiple datasets with an increasing number of classes, they do not explore the impact that the number of classes in the training sets has on the OOD detection performance. Additionally, this work does not consider some OOD detection methods that exploit geometric properties in the feature space such as NNGuide (Park et al., 2023), fDBD (Liu & Qin, 2023) or CTM (Ngoc-Hieu et al., 2023).

In a more theoretically grounded effort, Jaeger et al. (2022) identifies that conceptually similar problems such as misclassification detection, OOD detection, selective classification, and uncertainty quantification have heterogeneous task definitions and incompatible benchmarks. Accordingly, this work advocates for a unified evaluation framework centered on failure detection using confidence scoring functions (CSFs), with the Area Under the Risk-Coverage Curve (AURC) (Geifman et al., 2018) providing a holistic metric. Additionally, Jaeger et al. (2022) provides a codebase, coined *FD-Shifts*, which benchmarks a suite of CSFs across multiple datasets and diverse shifts (covariate, semantic), reporting that simple baselines like MSR often outperform complex methods. Traub et al. (2024), however, argued that the reliance of the AURC on selective risk at fixed thresholds does not adequately reflect holistic system performance. In response, they introduce a novel metric, the Area Under the Generalized Risk-Coverage Curve (AUGRC), which aggregates misclassification risk across all thresholds and better captures the joint probability of failure and its acceptance, fixing the limitations of the AURC. Both studies evaluate CIFAR-10 and CIFAR-100, considering multiple distribution shifts, but do not identify any dependence of the OOD detection performance on the number of classes in the training sets.

In a more applied setting, Bungert et al. (2023) explore *silent failures* in the classification of medical images. The authors benchmark various CSFs under realistic distribution shifts such as corruption (e.g. noise), acquisition (e.g. multiple data sources), and manifestation (e.g. unseen forms of a pathology) shifts. This study builds four biomedical imaging datasets, combining in some cases multiple sources, including dermoscopy, chest radiograph, fluorescence microscopy, and CT of lung nodules. This study highlights that none of the advanced CSFs obtained from different selective classification approaches such as DeepGamblers (Liu et al., 2019), ConfidNet (Corbière et al., 2019; Corbiere et al., 2021), or Monte Carlo Dropout (Gal & Ghahramani, 2016) (MCD) variants (CSFs obtained from predictions generated

¹Code is available at https://anonymous.4open.science/r/ood_systematic-C990/

by MCD activated at inference time) consistently outperform the MSR baseline. Although MCD-MSR performs best on average, results vary significantly depending on the data set and the type of shift, revealing trade-offs. In other words, this work emphasizes that a CSF that performs well under one domain shift may perform poorly under another. This highlights the difficulty in developing CSFs that generalize reliably in diverse biomedical conditions. Moreover, the choice of AURC as the main in this study may have hidden some trends in the performance of the CSFs.

Also in the medical domain, Gutbrod et al. (2025) established OpenMIBOOD, a medical benchmark spanning 14 datasets. They evaluated 24 post-hoc OOD detection methods, including classification-based, feature-based, and hybrid approaches, using standard metrics such as AUROC, FPR@95, and the harmonic mean of AUPR-IN and AUPR-OUT. The results reveal that methods effective on natural image benchmarks often fail in medical domains, with feature-based approaches outperforming probabilistic-based approaches across most scenarios. The authors highlight that covariate shift detection is more tractable than semantic shift detection in medical imaging. Furthermore, methods such as Residual and ViM (Wang et al., 2022), while successful on natural image benchmarks, exhibit inconsistent performance in medical data sets. A key insight is that medical imaging tasks often involve lower data variance and fewer classes, favoring methods that exploit deep feature representations over those that rely on probabilistic predictions.

3. Methods

3.1. Definitions and Notations

We consider a supervised classification problem where each input sample is denoted by $\mathbf{x} \in \mathcal{X}$, and its corresponding label is $y \in \mathcal{Y} = \{1, \dots, C\}$, representing one of C possible classes. The training dataset is defined as $\mathcal{D} = \{(\mathbf{x}_i, y_i)\}_{i=1}^N$, the test set as $\mathcal{D}^{\text{test}} = \{(\mathbf{x}_i^{\text{test}}, y_i^{\text{test}})\}_{i=1}^{N^{\text{test}}}$, and an out-of-distribution (OOD) dataset as $\mathcal{D}^{\text{OOD}} = \{(\mathbf{x}_i^{\text{OOD}}, 0)\}_{i=1}^{N^{\text{OOD}}}$, which contains samples not belonging to any of the known classes. For a given class $c \in \mathcal{Y}$, we define the subset of data corresponding to that class within a set \mathcal{D} as $\mathcal{D}_c = \{(\mathbf{x}, y) \in \mathcal{D} \mid y = c\}$, with cardinality $N_c = |\mathcal{D}_c|$.

We denote the classifier as a neural network function $f : \mathcal{X} \rightarrow \mathbb{R}^C$ parameterized by weights and biases $\mathcal{W} = \{(\mathbf{W}_1, \mathbf{b}_1), \dots, (\mathbf{W}_L, \mathbf{b}_L)\}$. This model is decomposed into an encoder $h : \mathcal{X} \rightarrow \mathbb{R}^D$, defined by layers up to $L-1$, and a linear classifier head $g : \mathbb{R}^D \rightarrow \mathbb{R}^C$ parametrized by the weights in the L -th layer. The complete model is composed as $f(\mathbf{x}) = (g \circ h)(\mathbf{x})$. For a given input \mathbf{x} , the penultimate-layer representation is $\mathbf{h} = h(\mathbf{x}) \in \mathbb{R}^D$, and

the classifier outputs a logit vector via $g(\mathbf{h}) = \mathbf{W}_L \mathbf{h} + \mathbf{b}_L$, where $\mathbf{W}_L = [\mathbf{w}_{1L}, \dots, \mathbf{w}_{CL}] \in \mathbb{R}^{C \times D}$ and $\mathbf{b}_L = [b_{1L}, \dots, b_{CL}] \in \mathbb{R}^C$. Let \mathbf{w} and \mathbf{W} represent the classifier weights, where we are intentionally omitting the layer-specific index L for simplicity in the current context. The predicted class is $\hat{y} = m(\mathbf{x}) = \arg \max_c [f(\mathbf{x})]_c$, and the softmax-based class probabilities are given by $p(\mathbf{x}) = \mathbf{p} = \frac{1}{\sum_j \exp(f(\mathbf{x})_j)} [\exp(f(\mathbf{x})_1), \dots, \exp(f(\mathbf{x})_C)] = \text{softmax}(f(\mathbf{x})) = \text{softmax}(g(\mathbf{h}))$.

We define the matrix of penultimate-layer activations for a dataset \mathcal{D} of size N as $\mathbf{H} = [\mathbf{h}_1, \dots, \mathbf{h}_N]^\top \in \mathbb{R}^{N \times D}$, and the corresponding matrix for class c as $\mathbf{H}_c = [\mathbf{h}_{i,c} : \mathbf{x}_i \in \mathcal{D}_c, i = 1, \dots, N_c]^\top \in \mathbb{R}^{N_c \times D}$. The global mean of the features is $\boldsymbol{\mu} = \frac{1}{N} \sum_{1 \leq i \leq N} \mathbf{h}_i = \frac{1}{N} \sum_{1 \leq i \leq N} h(\mathbf{x}_i)$, and the mean of the c -th class is $\boldsymbol{\mu}_c = \frac{1}{N_c} \sum_{\substack{1 \leq i \leq N_c \\ \mathbf{x}_i \in \mathcal{D}_c}} \mathbf{h}_{i,c} = \frac{1}{N_c} \sum_{\substack{1 \leq i \leq N_c \\ \mathbf{x}_i \in \mathcal{D}_c}} h(\mathbf{x}_i)$. These quantities also permit a geometric analysis of the last-layer representation via neural collapse metrics; see Appendix D.

3.2. Projection Filtering

Leveraging the observation that image data lies on low-dimensional manifolds (Pope et al., 2021)), we use Principal Component Analysis (PCA) to filter noise and capture intrinsic dimensionality. Principal Component Analysis (PCA) offers a principled way to exploit this low intrinsic dimensionality by filtering out directions in the data that are unlikely to carry meaningful signal, assuming that the true structure of the data is concentrated along a few high-variance directions, whereas noise is distributed more evenly across all dimensions. More specifically, the set of penultimate-layer activations \mathbf{H} are centered by subtracting the mean of each feature: $\tilde{\mathbf{H}} = \mathbf{H} - \mathbf{1}_N \boldsymbol{\mu}^\top$. The empirical covariance matrix $\boldsymbol{\Sigma} = \frac{1}{N} \tilde{\mathbf{H}}^\top \tilde{\mathbf{H}}$ is then decomposed as $\boldsymbol{\Sigma} = \mathbf{V} \boldsymbol{\Lambda} \mathbf{V}^\top$, where \mathbf{V} contains the eigenvectors and $\boldsymbol{\Lambda}$ is the diagonal matrix of eigenvalues $\lambda_1 \geq \lambda_2 \geq \dots \geq \lambda_D$. To denoise the data, only the top k principal components $\mathbf{P} = [\mathbf{v}_1, \dots, \mathbf{v}_k] \in \mathbb{R}^{D \times k}$, which span a subspace that captures most of the variance. The number of components k is decided so that certain percentage of variance is preserved at least. PCA can be applied to both the set of training activations \mathbf{H} centered by the global mean $\boldsymbol{\mu}$, from which \mathbf{P} is obtained, and the set of training activations for a given class c , \mathbf{H}_c , centered by its class mean $\boldsymbol{\mu}_c$, from which \mathbf{P}_c is computed.

For a new sample \mathbf{x}_* , the corresponding penultimate-layer activation \mathbf{h}_* is projected onto this subspace: $\mathbf{z}_* = \mathbf{P}^\top (\mathbf{h}_* - \boldsymbol{\mu}) = \mathbf{P}^\top \tilde{\mathbf{h}}_* \in \mathbb{R}^k$, and then reconstructed as $\hat{\mathbf{h}}_* = \mathbf{P} \mathbf{z}_* + \boldsymbol{\mu}$. This reconstruction preserves the dominant low-rank structure while discarding low-variance directions. Given that we have global and class subspaces, \mathbf{P} and \mathbf{P}_c respectively, we evaluate six projections: Global

projection: $\hat{\mathbf{h}} = \mathbf{P}\mathbf{P}^\top(\mathbf{h} - \boldsymbol{\mu}) + \boldsymbol{\mu}$; Class projection: $\hat{\mathbf{h}}_c = \mathbf{P}_c\mathbf{P}_c^\top(\mathbf{h} - \boldsymbol{\mu}_c) + \boldsymbol{\mu}_c$; Class predicted projection: $\hat{\mathbf{h}}_y$; Class projected logit: $\hat{\mathbf{g}}^{\text{class}} = [\hat{g}_1, \dots, \hat{g}_C]$, where $\hat{g}_c = \mathbf{w}_{cL}^\top \hat{\mathbf{h}}_c + b_{cL}$; Global projected probabilities: $\hat{\mathbf{p}} = \text{softmax}(g(\hat{\mathbf{h}}))$; and Class projected probabilities: $\hat{\mathbf{p}}^{\text{class}} = \text{softmax}(\hat{\mathbf{g}}^{\text{class}})$. A summary of the combination of these projections with possible OOD detection methods is in Appendix A. We later measure how such projections affect neural-collapse metrics (e.g., within-class variability and prototype angularity), and relate these changes to shifts in detector performance in Appendix D.

3.3. CLIP-based OOD Aggregation

We quantify distributional proximity to an OOD image dataset using the feature space from a CLIP model (Radford et al., 2021). Concretely, we extract L2-normalized image embeddings for both ID and candidate OOD sets using a fixed CLIP encoder under identical preprocessing. We then compute two label-agnostic distances between the empirical feature distributions: Fréchet distance (FD) (Dowson & Landau, 1982; Fréchet, 1957) and Maximum Mean Discrepancy (MMD) (Gretton et al., 2006) with a polynomial kernel. Both are evaluated on CLIP embeddings yielding global measures of how close the OOD distribution lies to the ID manifold; by construction, lower values indicate greater proximity. To capture class-aware proximity, we complement the global measures with two class-conditional distances. First, we represent each ID class by an image-embedding centroid and score a sample by its nearest-centroid angular distance in CLIP feature space. Second, we form text prototypes via prompt ensembling for each ID class (e.g., a photo of a class), embed them with the CLIP text model, and use the maximum image-text cosine similarity. For both class-conditional distances we compute the mean value to quantify a single metric that represents distance to the ID manifold. All four metrics are oriented so lower implies closer. Finally, we cluster these measurements using KMeans to derive near/mid/far proximity buckets. This protocol is model-agnostic with respect to the downstream OOD detector and applies unchanged to any choice of ID label space. Table 1 shows the resulting clustering and CLIP-derived distances for each dataset are reported in Appendix B.

3.4. Neural-collapse Geometry of Last-Layer features

We analyze the geometry of the last-layer representation through the lens of Neural Collapse (NC). Let $\tilde{\boldsymbol{\mu}}_c = \boldsymbol{\mu}_c - \boldsymbol{\mu}$ be the class-centered mean, $\cos_{\boldsymbol{\mu}}(c, c') = \frac{\tilde{\boldsymbol{\mu}}_c^\top \tilde{\boldsymbol{\mu}}_{c'}}{\|\tilde{\boldsymbol{\mu}}_c\|_2 \|\tilde{\boldsymbol{\mu}}_{c'}\|_2}$ be the cosine similarity between any pair of class-centered means c and c' , $\cos_{\mathbf{w}}(c, c') = \frac{\mathbf{w}_c^\top \mathbf{w}_{c'}}{\|\mathbf{w}_c\|_2 \|\mathbf{w}_{c'}\|_2}$ be the cosine similarity between any pair of classifier weights c and

Table 1. OOD dataset clustering. For each source dataset, the corresponding OOD datasets are categorized in near, mid and far datasets based on the CLIP-derived distances.

Source	Near	Mid	Far
CIFAR-10	CIFAR-100, TinyImagenet	iSUN, LSUN(r), LSUN(c), SVHN	Places365, Textures
SuperCIFAR-100	CIFAR-10, TinyImagenet	iSUN, LSUN(r), LSUN(c), SVHN	Places365, Textures
CIFAR-100	CIFAR-10, TinyImagenet	iSUN, LSUN(r), LSUN(c), SVHN	Places365, Textures
Tiny-Imagenet	CIFAR-10, CIFAR-100, iSUN, LSUN(r), LSUN(c)	Places365, Textures	SVHN

c' , $\Sigma_{\mathbf{W}} = \text{Avg}_{i,c}(\mathbf{h}_{i,c} - \boldsymbol{\mu})(\mathbf{h}_{i,c} - \boldsymbol{\mu})^T$ be the within-class covariance, $\Sigma_B = \text{Avg}_c(\tilde{\boldsymbol{\mu}}_c \tilde{\boldsymbol{\mu}}_c^T)$ be the between-class covariance, \dagger be the Moore-Penrose pseudoinverse, and $\mathbf{M} = [\tilde{\boldsymbol{\mu}}_c : c = 1, \dots, C]$ be the centered class-mean matrix. Neural Collapse is classically characterized by four phenomena in the terminal phase of training: (NC1) Variability collapse, (NC2) Convergence to simplex equiangular tight frame (ETF), (NC3) Convergence to self-duality, and (NC4) Simplification to nearest class center (NCC). Following (Papyan et al., 2020), we operationalize proximity to NC using five empirical metrics: **1**) Equinormness of the class means and the classifier weights: $\frac{\text{Std}_c(\|\tilde{\boldsymbol{\mu}}_c\|_2)}{\text{Avg}_c(\|\tilde{\boldsymbol{\mu}}_c\|_2)}$ and $\frac{\text{Std}_c(\|\mathbf{w}_c\|_2)}{\text{Avg}_c(\|\mathbf{w}_c\|_2)}$, **2**) Equiangularity of the class means and the classifier weights: $\text{Std}_{c,c' \neq c}(\cos_{\boldsymbol{\mu}}(c, c'))$ and $\text{Std}_{c,c' \neq c}(\cos_{\mathbf{w}}(c, c'))$, **3**) Maximal Equiangularity of the class means and the classifier weights: $(\cos_{\boldsymbol{\mu}}(i, j) = -\frac{1}{C-1})$: $\text{Avg}_{c,c'}|\cos_{\boldsymbol{\mu}}(c, c') + \frac{1}{C-1}|$ and $(\cos_{\mathbf{w}}(i, j) = -\frac{1}{C-1})$: $\text{Avg}_{c,c'}|\cos_{\mathbf{w}}(c, c') + \frac{1}{C-1}|$, **4**) Variability Collapse: $\frac{1}{C} \text{Tr}(\Sigma_{\mathbf{W}} \Sigma_B^\dagger)$, **5**) Self-duality: $2 - 2 \frac{\text{Tr}(\mathbf{W}\mathbf{M})}{\|\mathbf{W}\|_F \|\mathbf{M}\|_F}$. We compute these metrics for each backbone–dataset pair under three representation regimes: (i) unfiltered activations, (ii) global projection, and (iii) class-predicted projection. This yields a compact quantitative summary of how close each trained model is to an NC-like regime, and how projection filtering changes the effective geometry.

4. Results

4.1. Experimental Setup

We adopt the FD-Shifts protocol (Jaeger et al., 2022; Traub et al., 2024), which benchmarks CSFs across diverse failure sources and architectures. We consider the following CSF methods: Maximum Softmax Response (MSR) (Hendrycks & Gimpel, 2016), Generalized Entropy (GEN) (Liu et al., 2023) and Renyi Entropy (REN), Predictive Collision Entropy (PCE), GradNorm (Huang et al., 2021), Guessing Entropy (GE), PCA Reconstruction Error (Guan et al.,

2023), Class-Typical Matching (CTM) and Class-Typical Matching with mean class features (CTMmean) (Ngoc-Hieu et al., 2023), Residual and Virtual Logit Matching (ViM) (Wang et al., 2022), Maximum Logit Score (MLS) (Hendrycks et al., 2019), Nearest Neighbor Guidance (NNGuide) (Park et al., 2023), Neural Collapse-based OOD detection (NeCo) (Ammar et al., 2023), Energy (Liu et al., 2020), Kernel PCA Reconstruction Error (Fang et al., 2025), fast Decision Boundary Decision (fDBD) (Liu & Qin, 2023), Mahalanobis Distance (Maha) (Lee et al., 2018), predictive Normalized Maximum Likelihood (pNML) (Bibas et al., 2021), Confidence (from ConfidNet (Corbiere et al., 2021), DeVries (DeVries & Taylor, 2018), and Deep Gamblers (Liu et al., 2019) training paradigms). VGG-13 and ViT backbone models are trained from scratch and finetuned, respectively, on CIFAR-10, CIFAR-100, SuperCIFAR-100, and TinyImagenet. See Appendix E for hyperparameters. Monte-Carlo Dropout variants (MCD) of the scores named previously are also evaluated, for which we draw 50 stochastic forward passes at test time. Results are reported on ID test sets and OOD data sets, which are categorized based on CLIP-derived distances. When evaluating OOD detection, we compare OOD samples against only the correctly classified in-distribution (ID) samples and discard ID mistakes, so that a CSF is not rewarded for flagging ordinary in-distribution errors as if they were OOD. Misclassification detection is evaluated separately on the ID test set by ranking correct vs incorrect ID predictions to reflect the classifier’s accuracy.

4.2. Statistical Tests

We choose a Friedman test to compare CSFs in terms of their paired performances across blocks defined by the OOD dataset, training paradigm, source, and metric. The Friedman test is a nonparametric, blocked test that converts metric in each block to ranks, which is appropriate for CSF evaluation, where distributions are skewed, heteroscedastic, and not commensurate across blocks (the raw metric scales such as AUGRC or AURC can differ markedly across datasets). The null hypothesis is that the average ranks are the same across methods. If the null hypothesis is rejected, indicating metrics have different distribution of ranks, we need to determine which groups of CSFs have statistically indistinguishable performance. To achieve this, pairwise differences between CSFs while controlling multiplicity over all pairs are needed. Among rank-based post-hocs approaches, Conover (with Holm correction) provides sharper pairwise calls under the same nonparametric framework. From those adjusted p-values, we construct an Indifference Graph which connects two methods if they are not significantly different. Applying the Bron–Kerbosch algorithm enumerates all maximal sets of CSFs mutually indistinguishable so that top groups of CSFs are generated rather than a brittle sin-

gle winner. This clique view is faithful to the inferential decisions and naturally handles overlaps (a method can belong to multiple near-optimal sets). Detailed procedure and simplified example are described in Appendix C.

4.3. Top Cliques

Figure 1 (left) depicts Conover-Holm top cliques (at $\alpha = 0.05$) across evaluation regimes, with columns denoting settings (e.g., $\text{cifar10} \rightarrow \text{near}$, $\text{cifar100} \rightarrow \text{ID}$, $\text{tinyimagenet} \rightarrow \text{far}$) and rows corresponding to confidence-scoring functions (CSFs) when VGG-13 is the model backbone. Within each column, connected markers indicate the set of methods that are mutually indistinguishable from the best; larger cliques imply broader statistical ties, whereas smaller cliques indicate sharper separation. Shaded bands highlight persistent coalitions that reappear as winners across multiple regimes. In the $\text{source} \rightarrow \text{test}$ (ID) regime, which corresponds to misclassification detection, probability-based CSFs such as GEN and MSR dominate: the softmax geometry aligns well with error, with correctly classified ID examples exhibiting low predictive entropy, allowing simple confidence/energy scores to rank errors effectively without class-conditional structure.

Across *near* shifts, ENERGY, MLS, and NNGUIDE (especially the global variant) consistently appear in the top cliques. As the semantic distance from the source increases and the number of classes grows (e.g., cifar100 , tinyimagenet), these confidence-style scores become less dominant; geometry-aware CSFs such as FDBD and CTM increasingly anchor the winning sets, reflecting the greater value of boundary proximity and class-typicality under stronger shifts. Notably, CTM is repeatedly selected for tinyimagenet (200 classes), consistent with prototype-style scoring benefiting from richer class granularity, while NNGUIDE (global) is among the most frequently retained variants overall, indicating that aggregating neighborhood evidence globally improves OOD discrimination. Finally, as class count rises and shift strength increases from $\text{test} \rightarrow \text{far}$, clique sizes tend to contract, underscoring that detector performance depends sensitively on source-label cardinality and shift severity, with fewer methods remaining statistically tied at the top in the harder regimes.

Figure 1 (right) reports Conover-Holm top cliques at $\alpha = 0.05$ for a ViT backbone. Consistent with the analysis for top cliques when the backbone is VGG-13, in the $\text{source} \rightarrow \text{test}$ (misclassification) regime, the best-performing confidence-scoring functions (CSFs) are predominantly probabilistic: GEN, MSR, PCE, and REN appear in the top cliques across class counts. In contrast to the CNN case, CTM contributes less in the *mid* and *far* regimes. A plausible explanation is that CTM relies on class feature prototypes whose utility can diminish after fine-tuning a

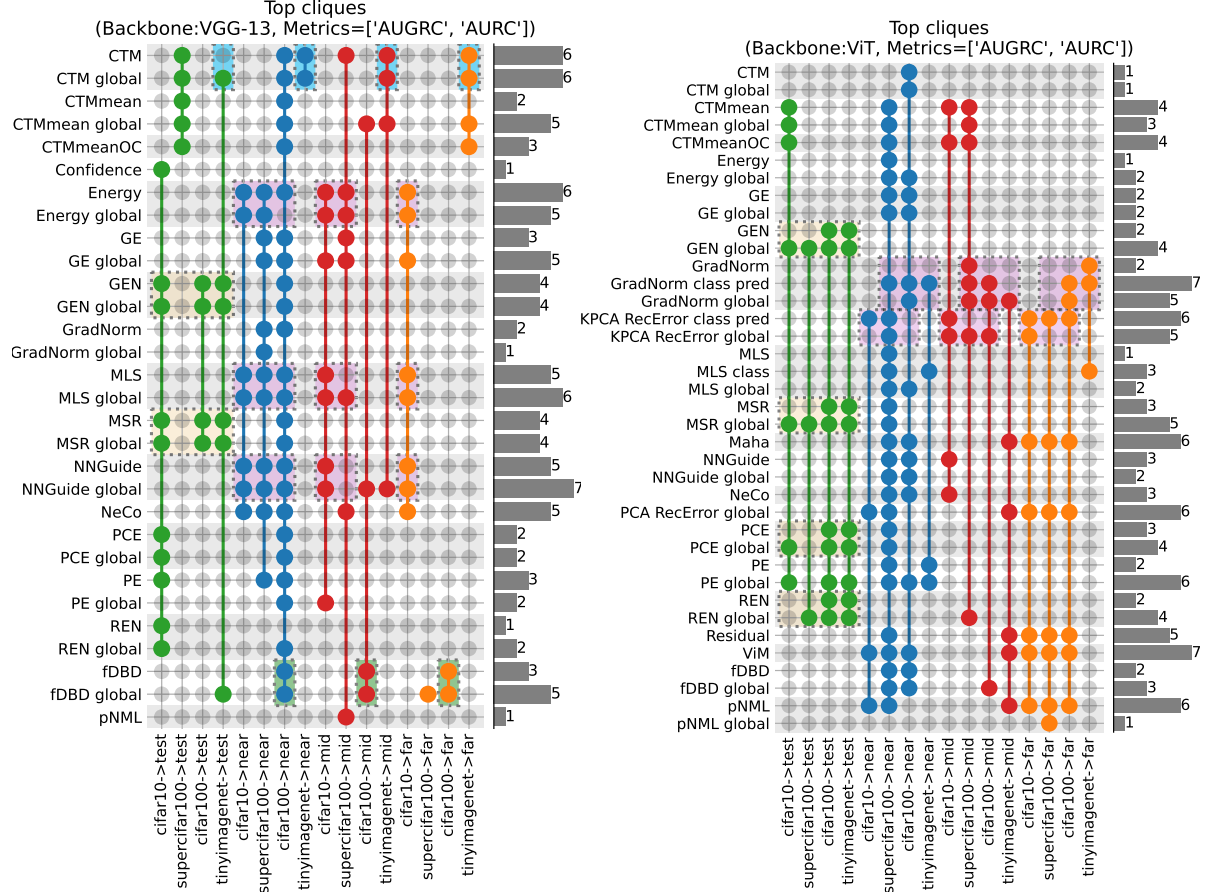


Figure 1. Top-clique map for AURC/AUGRC metrics: rows are CSF; columns are evaluation regimes labeled “source → test, near, mid, far”. Within each column, connected dots indicate the Conover–Holm top clique ($\alpha=0.05$). Larger cliques imply more methods are statistically tied. Shaded bands emphasize methods that repeatedly appear in top cliques across regimes. (Left) For VGG-13, probabilistic-derived CSF dominate the ID regime (“test”,) and prototype/geometry-aware methods (CTM-family, NNGuide, fDBD) dominate the mid/far regimes. (Right) For ViT, the ID regime is also dominated by probabilistic-derived CSFs, but top groups across near, mid, and far are centered on GradNorm and KPCA RecError.

large, pretrained ViT. Fine-tuning sharpens decision boundaries for the *source* task while partially reshaping prototype geometry, reducing CTM’s discriminative advantage under stronger shifts. Two methods that remain consistently competitive are GRADNORM and KPCA RECERROR; in our results, GRADNORM improves as the number of classes grows (larger label spaces yield tighter, more curved decision regions where gradient-based margin proxies are informative), whereas KPCA is comparatively stronger at smaller class counts (lower intrinsic dimensionality makes reconstruction error more stable).

Across *near*, *mid*, and *far* shifts, the *near* columns retain the largest cliques, while *mid* and *far* typically admit fewer top-tied CSFs. This mirrors the observation that, under fine-tuning, *mid* and *far* shifts present similar difficulty. Pre-training exposes ViT to semantically related categories, and fine-tuning adjusts boundaries to the source classes while preserving partial structure from pretraining, limiting the

number of clearly superior CSFs as shift severity increases. Notably, using the *class-pred* projection, which is the subspace selected by the predicted class, boosts KPCA RECERROR, but specially GRADNORM, likely because this projection leverages the classifier’s own discrimination to choose a feature subspace where margin curvature better separate atypical examples. Finally, VIM shows a strong presence in *near* and *far* but not *mid*, consistent with its reliance on virtual-logit structure that is effective when the shift is either small (logit geometry remains reliable) or very large (clear separation), but less decisive in intermediate, confusable conditions.

4.4. Neural-Collapse–Based Analysis

We use the NC metrics from Section 3.4 to interpret the architecture- and training-dependent rankings of confidence scoring functions (CSFs). Full tables and per-dataset details are given in Supplementary Section D.

CNNs (VGG-13). For TinyImageNet, the last-layer features are close to an NC regime: within-class variability is small, class means and classifier weights are nearly equinorm/equiangular, and self-duality is strong. In this geometry, class prototypes μ_c and weights w_c almost coincide, and ID features concentrate near their corresponding class means. Cosine-based prototype scores such as CTM and neighbor-based scores such as NNGuide are then near-Bayes-optimal in feature space: ID points have cosine ≈ 1 to the correct prototype, while OOD points lie in angular gaps and achieve a strictly smaller maximum cosine. This matches the cliques, where CTM and NNGuide dominate. On CIFAR-100, where self-duality is weaker, boundary-distance methods such as fDBD also appear in the top cliques. When weights and means misalign, distance to the learned linear decision surface becomes a more faithful margin proxy than pure prototype alignment. Global projection filtering only slightly changes aggregate NC metrics but improves CTMmean global and NNGuide global on mid-OOD, consistent with PCA acting as an ID manifold projector that removes nuisance directions and sharpens angular/neighbor structure in the subspace most aligned with between-class variability. On CIFAR-10 with CNNs, the last-layer geometry is close to neural collapse with well-separated, roughly equinorm class means and weights, so the correct-class logit is consistently much larger than the others. In this regime, both Energy (log-sum-exp of logits) and MLS (maximum logit) act as stable margin-like scores, giving high, well-separated values for ID samples and lower, less concentrated values for OOD inputs.

Transformers (ViT). For the fine-tuned ViT, NC metrics show weaker collapse, less ETF-like class means, and poorer alignment between means and weights across all datasets. The representation retains richer pretraining structure, and the linear head does not implement a clean nearest-prototype classifier. In this regime, prototype geometry is a less reliable summary of the decision rule, and the cliques instead favor GradNorm and KPCA with global and class predicted projections. These scores aggregate information when class means are not well separated or tightly coupled to the classifier. Class-predicted projection on ViTs reduces within-class variability in predicted-class subspaces (improved NC1 locally) and particularly benefits GradNorm and KPCA reconstruction error by sharpening boundary curvature and class-specific manifolds.

Overall, the NC analysis sharpens our representation-centric conclusions: CNNs trained on many classes and approaching NC favor prototype- and boundary-based CSFs, whereas ViTs with weaker collapse favor gradient- and manifold-based CSFs; projection filtering nudges models along this continuum by refining the ID subspace geometry. Detailed NC metrics computations and additional case studies are

provided in Appendix D.

4.5. MCD vs non-MCD Performance

Table 2 presents a comprehensive evaluation of various model configurations and training methodologies for selective classification, with performance measured by the Area Under the Generalized Risk-Coverage (AUGRC) curve. Only the best performing scores for each source and ID/OOD datasets are shown.

The most prominent finding is the trade-off between standard inference and Monte Carlo Dropout (MCD) as a function of the number of classes. For datasets with a low number of classes (e.g., 10 classes), models evaluated without MCD consistently achieve lower AUGRC scores. This suggests that for simpler tasks, methods that directly learn a confidence score, like those from the Deep Gamblers (DG) framework, are more effective at providing a reliable uncertainty estimate. However, as the number of classes increases, the performance of models evaluated with MCD improves significantly and often surpasses that of non-MCD methods. This indicates that for complex classification tasks, the epistemic uncertainty captured by MC dropout provides a more robust signal for selective classification.

The choice of training method is also critical for optimizing performance, with different approaches yielding the best results depending on the intended inference strategy. When using MCD for inference, models trained with ConfidNet produce the best AUGRC scores across the board. When MCD is not an option at inference time, the Deep Gamblers dg training method stands out. This end-to-end approach reframes selective classification as a gambling problem, learning to “abstain” from making a prediction when the confidence is low. This training method, however, requires tuning of the reward hyperparameter (see Appendix A). Our results show that this method produces the best AUGRC scores for non-MCD scenarios, regardless of whether dropout layers were used during training.

4.5.1. LIMITATIONS

Our study focuses on image classification with a restricted set of sources and shifts (CIFAR-10/100, super-CIFAR-100, TinyImageNet, and common near/mid/far OOD benchmarks), two backbone regimes (a scratch-trained CNN and a fine-tuned ViT), and a curated portfolio of confidence-scoring functions (CSFs). While this choice enables careful, paired comparisons and rigorous statistics, it limits external validity: results may not transfer to larger or newer backbones, self-supervised foundations, multi-label settings, detection/segmentation, or distribution drifts that are temporal, causal, or task-specific. Our CLIP-based grouping uses a fixed encoder and k -means with $k = 3$; both the encoder and clustering hyperparameters determine the “semantic

Table 2. Best IID (rows labeled test) and OOD (other rows) AUGRC scores and model configurations. This table summarizes the performance of various selective classification models, with results evaluated using the AUGRC metric. The findings demonstrate a clear dependence on dataset complexity. For datasets with a low number of classes, non-MCD methods, particularly the Deep Gamblers (DG) model, achieve superior AUGRC scores. Conversely, as the number of classes increases, Monte Carlo Dropout (MCD) with models trained using the **confidnet** method becomes the optimal approach.

	nonMCD AUGRC	MCD AUGRC	nonMCD paradigm	MCD paradigm
cifar10	3.9132	4.5384	DG	confidnet
	163.4954	163.3573	confidnet	confidnet
	149.7686	150.2396	confidnet	confidnet
	133.5868	133.8892	confidnet	confidnet
	148.6756	150.3665	DG	confidnet
	148.4497	148.7788	confidnet	confidnet
	159.3993	161.7047	DG	confidnet
superifar100	88.0191	89.9795	DG	DeVries
	287.3275	287.7814	DG	DeVries
	145.7328	144.6418	DG	DG
	266.3995	267.6652	confidnet	DG
	232.1150	225.5546	DG	DG
	221.0056	215.9046	DG	DG
	229.9232	234.8684	DG	confidnet
cifar100	237.1198	230.2041	DG	DG
	158.8078	162.8347	DG	confidnet
	264.2114	263.4520	DG	confidnet
	346.4916	354.0474	DG	confidnet
	54.3580	52.6486	DeVries	DG
	209.7024	209.9227	DeVries	DG
	195.6496	195.5451	confidnet	confidnet
tinyimagenet	181.3098	185.1370	DeVries	confidnet
	196.5520	194.7769	DG	confidnet
	196.2106	197.8931	DG	confidnet
	125.4978	121.1945	DeVries	confidnet
	210.3229	211.2779	DeVries	confidnet
	326.7164	322.6135	DG	confidnet
	97.0525	91.3660	DG	DG
tinyimagenet	219.9844	215.7338	confidnet	confidnet
	214.7156	209.2819	confidnet	confidnet
	195.8857	189.4729	DG	confidnet
	223.5343	218.2668	DG	DeVries
	211.7826	205.5667	DG	confidnet
	150.5724	146.8387	confidnet	confidnet
	209.3178	205.0045	DG	confidnet
tinyimagenet	344.5073	340.2405	DG	DeVries

distance.” In our evaluation, we emphasize threshold-free ranking metrics AURC/AUGRC, but do not fully explore cost-sensitive operating points, deployment-specific utility, or calibration–utility trade-offs under label shift. Finally, the ViT is fine-tuned from a large pretrained model; potential latent overlap with OOD categories was not exhaustively audited and could confound prototype-style scoring in subtle ways.

Our rank-based pipeline (Friedman → Conover with Holm correction → Bron–Kerbosch cliques) provides robust, multiple-comparison-controlled summaries, but inherits assumptions of complete blocks and exchangeability. Also, different post-hoc choices (e.g., Nemenyi, Quade, SC all-pairs) can yield slightly different borders for “indistinguishable” sets. Hyperparameter sweeps (e.g., DG rewards, kernel bandwidths for KPCA, temperature scaling, etc) were optimized on the validation set to achieve the best AUGRC,

and the best performing CSFs might change if another metric is used. Also, we did not evaluate computational cost or latency, which are factors that matter in deployment and may re-rank methods under real-time constraints.

4.6. Conclusion

Our study provides evidence that OOD detection performance is primarily governed by the structure of the learned representation rather than the sophistication of the scoring rule. Synthesizing the empirical results from our rank-based statistical pipeline with the theoretical insights from our Neural Collapse analysis, we summarize the key findings regarding architecture, training, and detection mechanisms as follows:

1. For Misclassification Detection (ID), simple probabilistic scores (GEN, MSR) consistently outperform specialized OOD detectors for both CNN and ViT models, confirming that softmax confidence remains the most reliable signal for identifying ordinary in-distribution prediction errors.
2. On CNNs, ranking quality is primarily driven by margin-based scores (Energy and MLS) which dominate in Near-OOD scenarios where logit magnitude is reliable, while geometry-aware scores (NNGuide, fDBD, CTM) dominate mid/far by leveraging distinct boundary proximity and feature-space clustering. On ViTs, efficacy shifts towards manifold and gradient-based approaches: GradNorm and KPCA Reconstruction Error remain consistently competitive across Near, Mid, and Far shifts, particularly when enhanced with class-predicted projection to navigate the complex, non-collapsed geometry of finetuned representations
3. Monte-Carlo Dropout yields a class-count–dependent trade-off (beneficial as the label space grows, less so on simple tasks).
4. Projection filtering enhances separability by filtering directions that do not support class-consistent structure, though the optimal strategy depends on the architecture: Global Projection sharpens angular geometry for CNNs (benefiting NNGuide and CTM), whereas Class-Predicted Projection is critical for finetuned ViTs to strip away pretraining residuals, enabling gradient- and manifold-based scores (GradNorm, KPCA) to perform effectively.
5. Our neural-collapse–based geometric analysis suggests that the apparent superiority of certain OOD detectors is largely a consequence of how training shapes prototype geometry and within-class collapse, providing a blueprint for designing representations that make failure detection easier.

Impact Statement

This paper presents a systematic benchmark and theoretical analysis of Out-of-Distribution (OOD) detection methods, with the goal of advancing the reliability and safety of machine learning systems. By identifying which detection scores perform best under specific architectures and training regimes, this work directly supports the deployment of more robust deep learning models in safety-critical applications, such as medical imaging and autonomous systems, where “silent failures” pose significant risks. While our primary contribution is methodological with theoretical insights, improved OOD detection capabilities can help mitigate automation bias and reduce the likelihood of high-confidence errors in real-world deployments. We do not foresee any immediate negative societal consequences or ethical concerns arising directly from this research.

References

Ammar, M. B., Belkhir, N., Popescu, S., Manzanera, A., and Franchi, G. Neco: Neural collapse based out-of-distribution detection. *ArXiv Preprint ArXiv:2310.06823*, 2023.

Bibas, K., Feder, M., and Hassner, T. Single layer predictive normalized maximum likelihood for out-of-distribution detection. *Advances In Neural Information Processing Systems*, 34:1179–1191, 2021.

Bron, C. and Kerbosch, J. Algorithm 457: Finding all cliques of an undirected graph. *Communications Of The ACM*, 16(9):575–577, 1973.

Bungert, T. J., Kobelke, L., and Jaeger, P. F. Understanding silent failures in medical image classification. In *International Conference On Medical Image Computing And Computer-Assisted Intervention*, pp. 400–410. Springer, 2023.

Conover, W. J. *Practical Nonparametric Statistics*. John Wiley & Sons, 1999.

Corbière, C., Thome, N., Bar-Hen, A., Cord, M., and Pérez, P. Addressing failure prediction by learning model confidence. *Advances In Neural Information Processing Systems*, 32, 2019.

Corbière, C., Thome, N., Saporta, A., Vu, T.-H., Cord, M., and Pérez, P. Confidence estimation via auxiliary models. *IEEE Transactions On Pattern Analysis And Machine Intelligence*, 44(10):6043–6055, 2021.

Cover, T. M. and Thomas, J. A. *Elements Of Information Theory (Wiley Series In Telecommunications And Signal Processing)*. Wiley-Interscience, USA, 2006. ISBN 0471241954.

Demšar, J. Statistical comparisons of classifiers over multiple data sets. *Journal Of Machine Learning Research*, 7 (Jan):1–30, 2006.

Deng, J., Dong, W., Socher, R., Li, L.-J., Li, K., and Fei-Fei, L. Imagenet: A large-scale hierarchical image database. In *2009 IEEE Conference On Computer Vision And Pattern Recognition*, pp. 248–255. Ieee, 2009.

DeVries, T. and Taylor, G. W. Learning confidence for out-of-distribution detection in neural networks. *ArXiv Preprint ArXiv:1802.04865*, 2018.

Dowson, D. and Landau, B. The fréchet distance between multivariate normal distributions. *Journal Of Multivariate Analysis*, 12(3):450–455, 1982.

Fang, K., Tao, Q., He, M., Lv, K., Yang, R., Hu, H., Huang, X., Yang, J., and Cao, L. Kernel PCA for out-of-distribution detection: Non-linear kernel selections and approximations. *ArXiv Preprint ArXiv:2505.15284*, 2025.

Fréchet, M. Sur la distance de deux lois de probabilité. In *Annales De L'ISUP*, volume 6, pp. 183–198, 1957.

Gal, Y. and Ghahramani, Z. Dropout as a bayesian approximation: Representing model uncertainty in deep learning. In *International Conference On Machine Learning*, pp. 1050–1059. PMLR, 2016.

Geifman, Y., Uziel, G., and El-Yaniv, R. Bias-reduced uncertainty estimation for deep neural classifiers. *ArXiv Preprint ArXiv:1805.08206*, 2018.

Granese, F., Romanelli, M., Gorla, D., Palamidessi, C., and Piantanida, P. Doctor: A simple method for detecting misclassification errors. *Advances In Neural Information Processing Systems*, 34:5669–5681, 2021.

Gretton, A., Borgwardt, K., Rasch, M., Schölkopf, B., and Smola, A. A kernel method for the two-sample-problem. *Advances In Neural Information Processing Systems*, 19, 2006.

Guan, X., Liu, Z., Zheng, W.-S., Zhou, Y., and Wang, R. Revisit PCA-based technique for out-of-distribution detection. In *Proceedings Of The IEEE/CVF International Conference On Computer Vision*, pp. 19431–19439, 2023.

Gutbrod, M., Rauber, D., Nunes, D. W., and Palm, C. Open-MIBOOD: Open medical imaging benchmarks for out-of-distribution detection. *ArXiv Preprint ArXiv:2503.16247*, 2025.

Hendrycks, D. and Gimpel, K. A baseline for detecting misclassified and out-of-distribution examples in neural networks. *ArXiv Preprint ArXiv:1610.02136*, 2016.

Hendrycks, D., Basart, S., Mazeika, M., Zou, A., Kwon, J., Mostajabi, M., Steinhardt, J., and Song, D. Scaling out-of-distribution detection for real-world settings. *ArXiv Preprint ArXiv:1911.11132*, 2019.

Holm, S. A simple sequentially rejective multiple test procedure. *Scandinavian Journal Of Statistics*, pp. 65–70, 1979.

Huang, R., Geng, A., and Li, Y. On the importance of gradients for detecting distributional shifts in the wild. *Advances In Neural Information Processing Systems*, 34: 677–689, 2021.

Iman, R. L. and Davenport, J. M. Approximations of the critical region of the fbietkan statistic. *Communications In Statistics-Theory And Methods*, 9(6):571–595, 1980.

Jaeger, P. F., Lüth, C. T., Klein, L., and Bungert, T. J. A call to reflect on evaluation practices for failure detection in image classification. *ArXiv Preprint ArXiv:2211.15259*, 2022.

Lee, K., Lee, K., Lee, H., and Shin, J. A simple unified framework for detecting out-of-distribution samples and adversarial attacks. *Advances In Neural Information Processing Systems*, 31, 2018.

Liu, L. and Qin, Y. Fast decision boundary based out-of-distribution detector. *ArXiv Preprint ArXiv:2312.11536*, 2023.

Liu, W., Wang, X., Owens, J., and Li, Y. Energy-based out-of-distribution detection. *Advances In Neural Information Processing Systems*, 33:21464–21475, 2020.

Liu, X., Lochman, Y., and Zach, C. Gen: Pushing the limits of softmax-based out-of-distribution detection. In *Proceedings Of The IEEE/CVF Conference On Computer Vision And Pattern Recognition*, pp. 23946–23955, 2023.

Liu, Z., Wang, Z., Liang, P. P., Salakhutdinov, R. R., Morency, L.-P., and Ueda, M. Deep gamblers: Learning to abstain with portfolio theory. *Advances In Neural Information Processing Systems*, 32, 2019.

Massey, J. L. Guessing and entropy. In *Proceedings Of 1994 IEEE International Symposium On Information Theory*, pp. 204. IEEE, 1994.

Ngoc-Hieu, N., Hung-Quang, N., Ta, T.-A., Nguyen-Tang, T., Doan, K. D., and Thanh-Tung, H. A cosine similarity-based method for out-of-distribution detection. *ArXiv Preprint ArXiv:2306.14920*, 2023.

Ovadia, Y., Fertig, E., Ren, J., Nado, Z., Sculley, D., Nowozin, S., Dillon, J., Lakshminarayanan, B., and Snoek, J. Can you trust your model’s uncertainty? evaluating predictive uncertainty under dataset shift. *Advances In Neural Information Processing Systems*, 32, 2019.

Papyan, V., Han, X., and Donoho, D. L. Prevalence of neural collapse during the terminal phase of deep learning training. *Proceedings Of The National Academy Of Sciences*, 117(40):24652–24663, 2020.

Park, J., Jung, Y. G., and Teoh, A. B. J. Nearest neighbor guidance for out-of-distribution detection. In *Proceedings Of The IEEE/CVF International Conference On Computer Vision*, pp. 1686–1695, 2023.

Pope, P., Zhu, C., Abdelkader, A., Goldblum, M., and Goldstein, T. The intrinsic dimension of images and its impact on learning. *ArXiv Preprint ArXiv:2104.08894*, 2021.

Radford, A., Kim, J. W., Hallacy, C., Ramesh, A., Goh, G., Agarwal, S., Sastry, G., Askell, A., Mishkin, P., Clark, J., et al. Learning transferable visual models from natural language supervision. In *International Conference On Machine Learning*, pp. 8748–8763. PMLR, 2021.

Rényi, A. On measures of entropy and information. In *Proceedings Of The Fourth Berkeley Symposium On Mathematical Statistics And Probability, Volume 1: Contributions To The Theory Of Statistics*, volume 4, pp. 547–562. University of California Press, 1961.

Shannon, C. E. A mathematical theory of communication. *The Bell System Technical Journal*, 27(3):379–423, 1948.

Traub, J., Bungert, T. J., Lüth, C. T., Baumgartner, M., Maier-Hein, K. H., Maier-Hein, L., and Jaeger, P. F. Overcoming common flaws in the evaluation of selective classification systems. *ArXiv Preprint ArXiv:2407.01032*, 2024.

Wang, H., Li, Z., Feng, L., and Zhang, W. ViM: Out-of-distribution with virtual-logit matching. In *Proceedings Of The IEEE/CVF Conference On Computer Vision And Pattern Recognition*, pp. 4921–4930, 2022.

Yang, J., Wang, P., Zou, D., Zhou, Z., Ding, K., Peng, W., Wang, H., Chen, G., Li, B., Sun, Y., et al. Openood: Benchmarking generalized out-of-distribution detection. *Advances In Neural Information Processing Systems*, 35: 32598–32611, 2022.

Zhang, J., Yang, J., Wang, P., Wang, H., Lin, Y., Zhang, H., Sun, Y., Du, X., Li, Y., Liu, Z., et al. Openood v1.5: Enhanced benchmark for out-of-distribution detection. *ArXiv Preprint ArXiv:2306.09301*, 2023.

Zhou, J., Jiang, J., and Zhu, Z. Are all layers created equal: A neural collapse perspective. In *The Second Conference On Parsimony And Learning (Proceedings Track)*, 2025.

A. Training Paradigms, CFS Baselines and Variations

A.1. Computing Infrastructure

All experiments were executed on an internal GPU cluster. *CNN* runs (VGG-13 trained from scratch) were scheduled on NVIDIA T4 GPUs, while *ViT* runs (fine-tuned from a large pretrained model) were scheduled on NVIDIA A100 GPUs. We did not mix GPU types within an experiment. Every training/evaluation job for a given backbone used the same GPU class to avoid hardware-induced variance.

A.2. Training Paradigms

A.2.1. CONFIDNET (REGRESSING THE TRUE-CLASS PROBABILITY).

Let $f_{\mathcal{W}} = g \circ h$ be a trained classifier with weights \mathcal{W} , logits $f(\mathbf{x}) \in \mathbb{R}^K$ and softmax $p_k(\mathbf{x}) = \exp(f_k(\mathbf{x}))/\sum_j \exp(f_j(\mathbf{x}))$. The standard confidence proxy is the maximum class probability, $\text{MSR}(\mathbf{x}) = \max_{k \in \{1, \dots, K\}} p_k(\mathbf{x})$, but this quantity can be spuriously large for both correct and erroneous predictions, hampering failure detection. ConfidNet replaces MSR with the *true-class probability* (TCP), $\text{TCP}(\mathbf{x}, y) = p_y(\mathbf{x})$, which is typically high for correct predictions and low for misclassifications (Corbière et al., 2019; Corbière et al., 2021). Because y is unknown at test time, ConfidNet learns an auxiliary regressor $s_{\mathcal{W}^{\text{conf}}} : \mathcal{X} \rightarrow [0, 1]$ that *predicts* $\text{TCP}(\mathbf{x}, y)$ from features of the trained classifier $f_{\mathcal{W}}$.

Denote by $E = h$ the encoder of $f_{\mathcal{W}}$ and by $g_{\mathcal{W}^{\text{conf}}} : \mathbb{R}^D \rightarrow [0, 1]$ a small MLP head. ConfidNet’s score is $s_{\mathcal{W}^{\text{conf}}}(\mathbf{x}) = (g_{\mathcal{W}^{\text{conf}}} \circ E)(\mathbf{x}) \approx \text{TCP}(\mathbf{x}, y)$, trained on the labeled training set $\mathcal{D}_{\text{train}}$ with a mean squared error loss $\mathcal{L}_{\text{conf}}(\mathcal{W}^{\text{conf}}; \mathcal{D}_{\text{train}}) = \frac{1}{|\mathcal{D}_{\text{train}}|} \sum_{(\mathbf{x}_i, y_i) \in \mathcal{D}_{\text{train}}} (s_{\mathcal{W}^{\text{conf}}}(\mathbf{x}_i) - \text{TCP}(\mathbf{x}_i, y_i))^2$. This *post-hoc* module transfers knowledge from the classifier’s encoder and yields a calibrated, label-informed confidence score at inference. It should be noted that the weights \mathcal{W} are kept frozen when training $g_{\mathcal{W}^{\text{conf}}}$. In practice, ConfidNet can be viewed as a supervised alternative to MSR that aligns the confidence target with the Bayes-relevant quantity TCP; see Corbière et al. (2019); Corbière et al. (2021) for more details on the implementation.

A.2.2. DEVRIES & TAYLOR: LEARNED CONFIDENCES VIA TARGET–PREDICTION INTERPOLATION.

Given a classifier $f_{\mathcal{W}} = g \circ h$ with softmax output $p(\mathbf{x}) \in \Delta^{K-1}$, DeVries & Taylor (2018) add a *confidence branch* in parallel to the class head. The branch shares features with the penultimate layer and outputs $s_{\mathcal{W}^{\text{devries}}}(\mathbf{x}) = \text{softmax}(\mathbf{w}^T h(\mathbf{x}) + b) \in [0, 1]$, interpreted as the network’s confidence that it can correctly predict the label of \mathbf{x} . During training, the method provides the network with “hints” by *interpolating* between its own prediction and the one-hot target \mathbf{y} according to s : $p'(\mathbf{x}, \mathbf{y}) = s_{\mathcal{W}^{\text{devries}}}(\mathbf{x}) p(\mathbf{x}) + (1 - s_{\mathcal{W}^{\text{conf}}}(\mathbf{x})) \mathbf{y}$. The task loss is then computed on p' rather than on p , e.g. the negative log-likelihood $\mathcal{L}_{\text{task}}(\mathcal{W}^{\text{devries}}, \mathcal{W}) = -\frac{1}{|\mathcal{D}_{\text{train}}|} \sum_{(\mathbf{x}_i, y_i)} \log ([p'(\mathbf{x}_i, \mathbf{y}_i)]_{y_i})$. Intuitively, when the model is *uncertain* ($s \approx 0$), it is allowed to rely more on the target distribution (a hint); when it is *confident* ($s \approx 1$), it must stand by its own prediction.

To avoid the degenerate solution $s = 0$ (which would always copy the target), a confidence regularizer encourages high s values: $\mathcal{L}_{\text{devries}}(\mathcal{W}^{\text{devries}}) = -\frac{1}{|\mathcal{D}_{\text{train}}|} \sum_{\mathbf{x}_i} \log s_{\mathcal{W}^{\text{conf}}}(\mathbf{x}_i)$, $\mathcal{L}_{\text{total}} = \mathcal{L}_{\text{task}} + \lambda \mathcal{L}_{\text{devries}}$, with $\lambda > 0$ balancing reliance on hints versus self-prediction. The resulting balancing where copying the target when the classifier struggles vs. being penalized for low confidence drives $s(\mathbf{x})$ to be large where the model is accurate and small where it is prone to error. At test time, the class prediction uses $p(\mathbf{x})$ from the base head, while $s(\mathbf{x})$ serves as a *confidence score* for failure/OOD detection; no hints are used at inference. See DeVries & Taylor (2018) for more details on the implementation.

A.2.3. DEEP GAMBLERS: ABSTENTION VIA A $(K+1)$ -ST CLASS AND A REWARD PARAMETER.

Liu et al. (2019) cast classification as a Kelly-style gambling game (Cover & Thomas, 2006). For a K -class task, the network predicts over $K+1$ outcomes. This means that an additional *abstain* option is attached to the original K labels. Let $f_{\mathcal{W}} = g \circ h$ with logits $f(\mathbf{x}) \in \mathbb{R}^{K+1}$, $p(\mathbf{x}) = \text{softmax}(f(\mathbf{x})) \in \Delta^K$, and write $p_k(\mathbf{x})$ for class $k \leq K$ and $p_{K+1}(\mathbf{x})$ for *abstain*. The training objective maximizes the expected (log) wealth in a horse-race with *reservation*: predicting the true class y yields payoff $o > 0$ (a tunable *reward*), and abstaining yields payoff 1. This leads to the loss $\mathcal{L}_{\text{DG}}(\mathcal{W}; \mathcal{D}_{\text{train}}, o) := -\frac{1}{|\mathcal{D}_{\text{train}}|} \sum_{(\mathbf{x}_i, y_i) \in \mathcal{D}_{\text{train}}} \log(o p_{y_i}(\mathbf{x}_i) + p_{K+1}(\mathbf{x}_i))$.

When $p_{K+1} = 0$ (no abstention), \mathcal{L}_{DG} reduces to cross-entropy up to an additive constant (since $\log o$ adds to the true-class

logit). The head is linear, $g(z) = Wz + b$, $W \in \mathbb{R}^{(K+1) \times D}$, $b \in \mathbb{R}^{K+1}$, so the method is a drop-in replacement for a standard classifier.

At test time, the model accepts an output if its (reward-weighted) probability dominates abstention, and rejects otherwise. A sufficient decision rule is $\text{accept} \Leftrightarrow o \cdot \max_{k \leq K} p_k(x) > p_{K+1}(x)$, reject (abstain) otherwise. Hence, larger o discourages abstention (the classifier must be more confident to reject), while smaller o encourages it. o is tuned on validation to meet a desired risk-coverage trade-off. For failure/OOD detection one can use the abstention mass as a score, $s_{\text{DG}}(x) = p_{K+1}(x)$ (higher \Rightarrow more likely atypical), or a margin-like variant $s_{\text{DG}}(x) = p_{K+1}(x) - o \cdot \max_{k \leq K} p_k(x)$ (negative \Rightarrow accept). The former is used in this work. The $(K+1)$ -st class thus implements a principled, calibrated abstention mechanism consistent with the Kelly criterion, while keeping the architecture and training pipeline simple. See Liu et al. (2019) for details on the implementation and effect of o .

Note

Unlike DeVries & Taylor (DeVries & Taylor, 2018) and Deep Gamblers (Liu et al., 2019), ConfidNet (Corbière et al., 2019; Corbière et al., 2021) fine-tunes a copy of a trained encoder h to generate the confidence score $s_{\mathcal{W}^{\text{conf}}}$. This copy does not modify f which is the output used to train and evaluate the ID/OOD detection methods. In fact, f in the ConfidNet training paradigm is the result of a *conventional* training approach, which is guided by the minimization of the cross-entropy loss.

A.3. ID/OOD Detection Methods

This section describes all the CSFs and their variations after applying the Projection Filtering described in section 3.2.

A.3.1. CLASS TYPICAL MATCHING (CTM) AND CLASS TYPICAL MATCHING WITH CLASS MEANS PROTOTYPES (CTMMEAN) (NGOC-HIEU ET AL., 2023)

Prototype matching in feature space consists of quantifying the similarity between a sample \mathbf{x} and the last-layer trained weights $\{\mathbf{w}_1, \dots, \mathbf{w}_K\}$. Therefore the similarity to the closest trained weight is $\text{CTM}(\mathbf{x}) = \max_{k \leq C} \text{sim}(\mathbf{w}_k, \mathbf{h})$. Alternatively, we can compute class means $\boldsymbol{\mu}_{\text{train}}^c$ and score by similarity to the closest class mean, $\text{CTMmean}(\mathbf{x}) = \max_{k \leq C} \text{sim}(\boldsymbol{\mu}_{\text{train}}^k, \mathbf{h})$. Following Ngoc-Hieu et al. (2023), we use cosine similarity in this work, where $\text{sim}(\mathbf{u}, \mathbf{v}) = \frac{\mathbf{u}^\top \mathbf{v}}{\|\mathbf{u}\|_2 \|\mathbf{v}\|_2}$. CTM scores the *typicality* of \mathbf{x} by comparing its feature \mathbf{h} against a bank of class representatives. Higher similarity indicates greater in-distribution (ID) conformity.

A.3.2. ENERGY (LIU ET AL., 2020)

The energy score is defined as $\text{Energy}(\mathbf{x}) = -T \log \sum_{k=1}^C \exp(g(\mathbf{h})_k/T)$, with temperature $T > 0$. Higher Energy score typically indicates higher uncertainty.

A.3.3. MAXIMUM SOFTMAX RESPONSE (MSR) (HENDRYCKS & GIMPEL, 2016) AND MAXIMUM LOGIT SCORE (MLS) (HENDRYCKS ET AL., 2019)

A baseline confidence score given by the maximum predicted probability $\text{MSR}(\mathbf{x}) = \max_{k \leq C} p_k$, widely used for OOD detection. Lower values indicate atypical inputs. Similarly, MLS is a confidence score measured in the logit space, $\text{MLS}(\mathbf{x}) = \max_{k \leq C} g(\mathbf{h})_k$, often more stable than softmax under temperature changes.

A.3.4. PREDICTIVE ENTROPY (PE), GENERALIZED ENTROPY (GEN), RENYI ENTROPY (REN), GUESSING ENTROPY (GE), AND PREDICTIVE COLLISION ENTROPY (PCE)

Predictive Entropy (PE) (Ovadia et al., 2019). Uncertainty via Shannon entropy (Shannon, 1948) of the predictive distribution $\text{PE}(\mathbf{x}) = H(p(\mathbf{x})) = -\sum_{k=1}^C p_k \log p_k$, with larger entropy signaling higher uncertainty.

Generalized Entropy (GEN) (Liu et al., 2023). GEN is a post-hoc OOD score that uses the softmax probabilities of a trained classifier. Let $\mathbf{p}_{(1)} \geq \dots \geq \mathbf{p}_{(K)}$ denote the probabilities sorted in descending order for a given input \mathbf{x} . For sensitivity and numerical stability in many-class settings, GEN truncates to the top- M classes and computes a generalized entropy with exponent $\gamma \in (0, 1)$: $\text{GEN}(\mathbf{x}) = \sum_{k=1}^M \mathbf{p}_{(k)}^\gamma (1 - \mathbf{p}_{(k)})^\gamma$. The confidence score is the *negated* generalized

entropy so that a larger GEN (lower entropy) indicates more ID-like predictions.

Rényi Entropy (REN). The Rényi entropy (Rényi, 1961) of order α is a smooth generalization of Shannon entropy that emphasizes different parts of the distribution. Similar to GEN, REN is defined by a truncation parameter M and exponent $\alpha \in (0, 1)$: $\text{REN}(\mathbf{x}) = \frac{1}{1-\alpha} \log \sum_{k=1}^M \mathbf{p}_{(k)}^\alpha$.

Guessing Entropy (GE). GE (Massey, 1994) quantifies the expected number of guesses to identify the true class when labels are guessed in decreasing probability $p_k(\mathbf{x})$: if $p_{(1)} \geq \dots \geq p_{(K)}$ are sorted, then $\text{GE}(\mathbf{x}) = \sum_{k=1}^C k \mathbf{p}_{(k)}$, with larger values denoting higher uncertainty.

Predictive Collision Entropy (PCE) (Granese et al., 2021). PCE measures prediction uncertainty via the *collision* (order-2 Rényi) entropy of the softmax distribution: $\text{PCE}(\mathbf{x}) = -\log \sum_{k=1}^C \mathbf{p}_k^2$. Since $\sum_k \mathbf{p}_k^2$ is the “collision probability,” PCE grows as the distribution spreads (uncertain/atypical) and shrinks as it peaks (confident/ID-like). This uncertainty score uses the entire predictive distribution rather than just its maximum.

A.3.5. MAHALANOBIS DISTANCE (MAHA) (LEE ET AL., 2018)

Assuming Gaussian class-conditional features, score by the (negative) Mahalanobis distance to the nearest class centroid is $\text{Maha}(\mathbf{x}) = \max_{k \leq C} (\mathbf{h}(\mathbf{x}) - \boldsymbol{\mu}_{\text{train}}^k)^\top \boldsymbol{\Sigma}^{-1} (\mathbf{h}(\mathbf{x}) - \boldsymbol{\mu}_{\text{train}}^k) = \bar{\mathbf{h}}_k^\top \boldsymbol{\Sigma}^{-1} \bar{\mathbf{h}}_k$, where $\boldsymbol{\Sigma}$ is the empirical covariance matrix.

A.3.6. NEAREST NEIGHBOR GUIDE (NNGUIDE) (PARK ET AL., 2023)

NNGuide is a post-hoc wrapper that modulates any classifier-based OOD score $S_{\text{base}}(\mathbf{h})$ using nearest neighbors from an ID bank of features. This bank is formed by sampling $\alpha \in (0, 1)$ of ID training features \mathbf{h}_i (L2-normalized) and their base scores $s_i = S_{\text{base}}(\mathbf{h}_i)$. More specifically, given an input \mathbf{x} , the corresponding feature \mathbf{h} (L2-normalized) defines a confidence-scaled similarity list $\{s_i \cos(\mathbf{h}, \mathbf{h}_i)\}_{i=1}^N$, which is sampled by taking the top- k terms, where $k = \lfloor \alpha N \rfloor$. The top- k terms set the guidance $G(\mathbf{h}) = \frac{1}{k} \sum_{i \leq k} s_i \cos(\mathbf{h}, \mathbf{h}_i)$, and the score NNGuide(\mathbf{x}) = $S_{\text{base}}(\mathbf{h}) \cdot G(\mathbf{h})$. In practice, S_{base} is the (negative) Energy score, but NNGuide can improve other classifier-based scores. Intuitively, $G(\mathbf{h})$ down-scales overconfident far-OOD points where cosine similarities are small and preserves near-ID points using high-confidence neighbors.

A.3.7. FAST DECISION BOUNDARY DETECTOR (FDBD) (LIU & QIN, 2023)

fDBD scores a sample by how far its feature lies from the nearest class decision boundary, regularized by feature deviation from the in-distribution mean. For each non-predicted class $c \neq m(\mathbf{x})$, the (unknown) distance in the feature space to the c -boundary is lower bounded by $D_g(\mathbf{h}, k) = \frac{|(\mathbf{w}_m - \mathbf{w}_k)^\top \mathbf{h} + (b_m - b_k)|}{\|\mathbf{w}_m - \mathbf{w}_k\|_2}$, i.e., the Euclidean distance from \mathbf{h} to the separating hyperplane between classes $m(\mathbf{x})$ and c . Averaging these distances and *regularizing* by the feature’s deviation from the ID mean $\boldsymbol{\mu}_{\text{train}}$ yields the score fDBD(\mathbf{x}) = $\frac{1}{C-1} \sum_{k=1}^C \sum_{k \neq m(\mathbf{x})} \frac{D_g(\mathbf{h}, k)}{\|\mathbf{h} - \boldsymbol{\mu}_{\text{train}}\|_2}$. The regularizer compares ID/OOD at equal deviation levels, empirically sharpening separation; the distance term captures that ID features tend to reside farther from decision boundaries than OOD features.

A.3.8. PREDICTIVE NORMALIZED MAXIMUM LIKELIHOOD (pNML) (BIBAS ET AL., 2021)

pNML treats a deep network as a fixed feature extractor and for each test samples computes a regret score by simulating in closed form the best last-layer update for every possible label. Given the matrix of normalized penultimate-layer training activations $\hat{\mathbf{H}} = [\mathbf{h}_1 / \|\mathbf{h}_1\|_2, \dots, \mathbf{h}_N / \|\mathbf{h}_N\|_2]$, the online-update direction \mathbf{g} via the kernel-range projection is $\mathbf{g} = \mathbf{h}_\perp / \|\mathbf{h}_\perp\|_2^2$ if $\mathbf{h}_\perp = (\mathbf{I} - \hat{\mathbf{H}}^\top \hat{\mathbf{H}}) \mathbf{h} \neq 0$; else $\mathbf{g} = \frac{\hat{\mathbf{H}}^\top \hat{\mathbf{H}}^\top \mathbf{h}}{1 + \mathbf{h}^\top \hat{\mathbf{H}}^\top \hat{\mathbf{H}}^\top \mathbf{h}} \mathbf{h}^C$, where $\hat{\mathbf{H}}^\top$ is the Moore–Penrose inverse of the normalized training activations. The pNML regret is $\text{pNML}(\mathbf{x}) = \log \sum_{k=1}^C \frac{\mathbf{p}_k}{\mathbf{p}_k + \mathbf{p}_k^\top \mathbf{g} (1 - \mathbf{p}_k)}$ and serves as an OOD/failure score (larger pNML \Rightarrow less trustworthy prediction). Intuitively, pNML is small when \mathbf{h} lies in the high-variance ID subspace or is far from decision boundaries (the genie’s label-specific update has little effect), and large otherwise.

A.3.9. GRADNORM (HUANG ET AL., 2021)

Given a trained classifier with softmax $p(\mathbf{x})$, GradNorm defines the OOD score as the vector norm of the gradients obtained by backpropagating the Kullback–Leibler divergence from a uniform target, i.e. $\text{GradNorm}(\mathbf{x}) = \|\partial_w \text{KL}(\mathbf{u} \parallel p(\mathbf{x}))\|_p = \left\| \frac{1}{C} \sum_{k=1}^C \frac{\partial \mathcal{L}_{\text{CE}}(g(\mathbf{h}), k)}{\partial \mathbf{w}} \right\|_p$, typically using the L_1 norm on the *last-layer* weights. This choice is label-agnostic and exploits that in-distribution inputs produce more *peaked* predictions and thus larger gradients than OOD inputs. A simple analysis shows $\text{GradNorm}(\mathbf{x})$ factorizes into a feature-space term and an output-space term, capturing joint information that improves separability over output-only scores.

A.3.10. PCA RECONSTRUCTION ERROR (PCA RECERROR) (GUAN ET AL., 2023)

PCA Reconstruction Error models the in-distribution feature manifold by fitting a low-dimensional principal subspace on penultimate features and scores a test example by the energy of its component orthogonal to that subspace, so larger residuals indicate atypicality. This approach computes the ID mean $\boldsymbol{\mu}$ and covariance $\boldsymbol{\Sigma}$, then takes the top- k eigenvectors \mathbf{U}_k of $\boldsymbol{\Sigma}$, and forms the projector $\mathbf{M} = \mathbf{U}_k \mathbf{U}_k^\top$. The *PCA reconstruction error* for a test point is $e(\mathbf{x}) = \|(\mathbf{I} - \mathbf{M})(\mathbf{h}(\mathbf{x}) - \boldsymbol{\mu})\|_2$, i.e., the energy of the component orthogonal to the ID principal subspace. Although intuitively $e(\mathbf{x})$ should be smaller on ID than OOD, a detailed analysis shows that $e(\mathbf{x})$ (i) mixes the angle between $\mathbf{h}(\mathbf{x}) - \boldsymbol{\mu}$ and the principal subspace and (ii) the norm $\|\mathbf{h}(\mathbf{x}) - \boldsymbol{\mu}\|_2$, which is typically *larger* for ID than OOD; this blurs separability for vanilla PCA-OOD. To mitigate the norm effect, a simple regularized score $r(\mathbf{x}) = \frac{\|\mathbf{h} - \hat{\mathbf{h}}\|_2}{\|\mathbf{h}\|_2}$, where $\hat{\mathbf{h}} = \hat{\mathbf{h}}(\mathbf{x}) = \mathbf{M}(\mathbf{h}(\mathbf{x}) - \boldsymbol{\mu}) + \boldsymbol{\mu}$, improves discrimination, and can be fused multiplicatively with logit-based scores.

A.3.11. KERNEL PCA RECONSTRUCTION ERROR (KPCA RECERROR) (FANG ET AL., 2025)

KPCA Reconstruction Error models the in-distribution (ID) feature manifold in a *non-linear* subspace and scores a test point by its reconstruction error in that subspace. To mitigate feature–norm imbalance and preserve useful Euclidean relations, KPCA first ℓ_2 –normalizes features $\hat{\mathbf{h}} = \mathbf{h}/\|\mathbf{h}\|_2$ and define a Gaussian kernel on the unit sphere $k(\mathbf{x}, \mathbf{x}') = \exp\left(-\frac{1}{2\sigma^2} \|\hat{\mathbf{h}} - \hat{\mathbf{h}}'\|_2^2\right) = \exp\left(-\frac{1}{\sigma^2} (1 - \cos(\hat{\mathbf{h}}, \hat{\mathbf{h}}'))\right)$, which can be viewed as a Cosine–Gaussian composition. Given ID training points, the centered Gram matrix is defined as $\mathbf{K}_c = \mathbf{H} \mathbf{K} \mathbf{H}$ with $\mathbf{K}_{ij} = k(\mathbf{x}_i, \mathbf{x}_j)$ and $\mathbf{H} = \mathbf{I} - \frac{1}{n} \mathbf{1} \mathbf{1}^\top$. Using the centered Gram matrix, KPCA solves the eigenproblem $\mathbf{K}_c \boldsymbol{\alpha}_m = n \lambda_m \boldsymbol{\alpha}_m$, where $m = 1, \dots, N$, and defines principal coordinates for a test point \mathbf{x} via the centered kernel $k_c(\mathbf{x}, \mathbf{x}_i) = k(\mathbf{x}, \mathbf{x}_i) - \frac{1}{n} \sum_j k(\mathbf{x}, \mathbf{x}_j) - \frac{1}{n} \sum_j k(\mathbf{x}_j, \mathbf{x}_i) + \frac{1}{n^2} \sum_{j \neq i} k(\mathbf{x}_j, \mathbf{x}_j)$: $\phi_m(\mathbf{x}) = \frac{1}{\sqrt{\lambda_m}} \sum_{i=1}^N \boldsymbol{\alpha}_{mi} k_c(\mathbf{x}, \mathbf{x}_i)$. The squared reconstruction error in feature space after projecting onto the top k components is $e(\mathbf{x}) = k_c(\mathbf{x}, \mathbf{x}) - \sum_{m=1}^k \phi_m(\mathbf{x})^2$. Similar to PCA Reconstruction Error, the larger $e(\mathbf{x})$ is, the more atypical \mathbf{x} becomes. A norm–regularized variant KPCA(\mathbf{x}) = $e(\mathbf{x})/\sqrt{k_c(\mathbf{x}, \mathbf{x})}$ further reduces residual norm confounds.

To avoid computing the full $N \times N$ kernel and $O(N^2)$ memory, we approximate the Gaussian on the sphere with an explicit map $\psi : \mathbb{R}^D \rightarrow \mathbb{R}^M$ so that $k(\mathbf{x}, \mathbf{x}') \approx \psi(\hat{\mathbf{h}})^\top \psi(\hat{\mathbf{h}}')$ with $M \ll N$. In particular, we use Nyström features with landmarks $\{\mathbf{x}_\ell^*\}_{\ell=1}^M$ (e.g., low-energy ID points near the boundary), $\psi(\hat{\mathbf{z}}) = C W^{-1/2}$ where $C_\ell = k(\mathbf{x}, \mathbf{x}_\ell^*)$ and W is the landmark Gram matrix. We then perform ordinary PCA on $\psi(\hat{\mathbf{h}})$: compute mean $\boldsymbol{\mu}$ and top- k eigenvectors \mathbf{U}_k of the empirical covariance, and score a test point by the Euclidean reconstruction error $\tilde{e}(\mathbf{x}) = \|(\mathbf{I} - \mathbf{U}_k \mathbf{U}_k^\top)(\psi(\hat{\mathbf{h}}) - \boldsymbol{\mu})\|_2^2$, and $\tilde{r}(\mathbf{x}) = \frac{\tilde{e}(\mathbf{x})}{\|\psi(\hat{\mathbf{h}})\|_2}$. Empirically, the Cosine–Gaussian kernel and the low-energy Nyström approximation improve separability and efficiency over linear PCA and nearest-neighbor baselines.

A.3.12. RESIDUAL PROJECTION AND VIRTUAL MATCHING LOGIT (ViM) (WANG ET AL., 2022)

Residual Projection score. If the ID principal subspace $P \subset \mathbb{R}^N$ from training features is defined as the span of the top- D eigenvectors of $\mathbf{H}^\top \mathbf{H}$, then $R \in \mathbb{R}^{N \times (N-D)}$ have columns spanning P^\perp . The *residual* projection of \mathbf{x} is $r(\mathbf{x}) = RR^\top \mathbf{h}$, and the residual projection score is $\text{Residual}(\mathbf{x}) = \|r(\mathbf{x})\|_2$, which increases as the feature departs from the ID principal subspace. This score is class-agnostic and leverages feature-space geometry that is lost when projecting to logits.

ViM (Virtual-logit Matching). ViM fuses the class-agnostic residual with class-dependent logits by creating a virtual $(K+1)$ -st logit from the residual and matching its scale to the real logits. ViM score is defined as the softmax probability of this virtual class: $\text{ViM}(\mathbf{x}) = \frac{\exp\{\ell_0(\mathbf{x})\}}{\sum_{k=1}^K \exp\{g(\mathbf{x})_k\} + \exp\{\ell_0(\mathbf{x})\}}$, where the virtual logit $\ell_0(\mathbf{x}) = \alpha \|r(\mathbf{x})\|_2$, and the scaling

factor $\alpha = \mathbb{E}_{\mathbf{x} \sim \text{ID}}[\max_{k \leq K} f_k(\mathbf{x})] / \mathbb{E}_{\mathbf{x} \sim \text{ID}}[\|r(\mathbf{x})\|_2]$. Equivalently, applying the transformation $t(x) = -\ln(1/x - 1)$ yields $t(\text{ViM}(\mathbf{x})) = \alpha \|r(\mathbf{x})\|_2 - \log \sum_{k=1}^K e^{g(\mathbf{h})_k}$, i.e., a residual term minus the *Energy* of the logits. Thus ViM is large when the residual is large and the (ID) logits are small.

A.3.13. NEURAL COLLAPSE (NeCo) (AMMAR ET AL., 2023)

This method is motivated by the Neural Collapse phenomena (Papyan et al., 2020), which unveils geometric properties that manifest at the end of the training process. NeCo's new observation establishes ID/OOD orthogonality, which implies that OOD features concentrate near the origin after projection onto the ID subspace. This method fits PCA on ID features to obtain the top- d principal directions $\mathbf{P} \in \mathbb{R}^{D \times d}$ (orthonormal columns). Then it scores an input by the normalized projection of its feature onto the ID principal subspace, $\text{NeCo}(\mathbf{x}) = \frac{\|\mathbf{P}^\top \mathbf{h}\|_2}{\|\mathbf{h}\|_2}$, so that ID points (well aligned with the ID subspace) yield larger scores, while OOD points (near-orthogonal to that subspace) yield smaller scores. This score is optionally calibrated by multiplying with MLS to inject class-scale information.

A.4. Methods Variations

As described in section 3.2, the global and class subspaces, \mathbf{P} and \mathbf{P}^c respectively, allow multiple projections that can be used to modify existing OOD detection methods. The following list shows possible modifications to the feature, logit and probability spaces, and table 3:

- **Global projection:** $\hat{\mathbf{h}} = \mathbf{P}\mathbf{P}^\top(\mathbf{h} - \boldsymbol{\mu}_{\text{train}}) + \boldsymbol{\mu}_{\text{train}}$
- **Class projection:** $\hat{\mathbf{h}}^c = \mathbf{P}^c\mathbf{P}^{c\top}(\mathbf{h} - \boldsymbol{\mu}_{\text{train}}^c) + \boldsymbol{\mu}_{\text{train}}^c$
- **Class averaged projection:** $\hat{\mathbf{h}}^{\text{avg}} = \frac{1}{C} \sum_{c=1}^C \hat{\mathbf{h}}^c$
- **Class predicted projection:** $\hat{\mathbf{h}}^{\text{pred}} = \hat{\mathbf{h}}^{\hat{y}}$, where $\hat{y} = m(\mathbf{x})$
- **Class projected logit:** $\hat{\mathbf{g}}^{\text{class}} = [\hat{g}^1, \dots, \hat{g}^C]$, where $\hat{g}^c = \mathbf{w}_{cL}^\top \hat{\mathbf{h}}^c + b_{cL}$
- **Global projected probabilities:** $\hat{\mathbf{p}} = \text{softmax}(g(\hat{\mathbf{h}}))$
- **Class projected probabilities:** $\hat{\mathbf{p}}^{\text{class}} = \text{softmax}(\hat{\mathbf{g}}^{\text{class}})$
- **Class-predicted probabilities:** $\hat{\mathbf{p}}^{\text{pred}} = \text{softmax}(g(\hat{\mathbf{h}}^{\text{pred}}))$
- **Class-averaged probabilities:** $\hat{\mathbf{p}}^{\text{avg}} = \text{softmax}(g(\hat{\mathbf{h}}^{\text{avg}}))$

B. CLIP-based OOD Aggregation

Let ϕ_{img} and ϕ_{text} be fixed CLIP encoders (Radford et al., 2021). For any image \mathbf{x} , define the ℓ_2 -normalized image embedding $\mathbf{z} = \tilde{\phi}_{\text{img}}(\mathbf{x}) = \phi_{\text{img}}(\mathbf{x}) / \|\phi_{\text{img}}(\mathbf{x})\|_2 \in \mathbb{R}^d$. Given an in-distribution set $\mathcal{D}_{\text{ID}} = \{\mathbf{x}_i, y_i\}_{i=1}^N$ and a candidate OOD set $\mathcal{D}_{\text{OOD}} = \{\mathbf{x}'_j\}_{j=1}^m$, we extract $Z_{\text{train}} = \{\mathbf{z}_i\}_{i=1}^n$ and $Z_{\text{OOD}} = \{\mathbf{z}'_j\}_{j=1}^m$ under identical preprocessing.

Global distances. We summarize each set by its empirical Gaussian in CLIP space with means and covariances $(\boldsymbol{\mu}_{\text{ID}}, \boldsymbol{\Sigma}_{\text{ID}})$ and $(\boldsymbol{\mu}_{\text{OOD}}, \boldsymbol{\Sigma}_{\text{OOD}})$, and compute the Fréchet distance (FD) (Dowson & Landau, 1982; Fréchet, 1957): $\text{FD}^2(\mathcal{D}_{\text{OOD}} \rightarrow \mathcal{D}_{\text{ID}}) = \|\boldsymbol{\mu}_{\text{ID}} - \boldsymbol{\mu}_{\text{OOD}}\|_2^2 + \text{Tr}(\boldsymbol{\Sigma}_{\text{ID}} + \boldsymbol{\Sigma}_{\text{OOD}} - 2(\boldsymbol{\Sigma}_{\text{ID}}^{1/2} \boldsymbol{\Sigma}_{\text{OOD}} \boldsymbol{\Sigma}_{\text{ID}}^{1/2})^{1/2})$.

As a second global measure, we compute the (unbiased) maximum mean discrepancy (MMD) (Gretton et al., 2006) with a polynomial kernel $k(\mathbf{u}, \mathbf{v}) = (\mathbf{u}^\top \mathbf{v} + c)^d$: $\widehat{\text{MMD}}^2 = \frac{1}{n(n-1)} \sum_{i \neq i'} k(\mathbf{z}_i, \mathbf{z}_{i'}) + \frac{1}{m(m-1)} \sum_{j \neq j'} k(\mathbf{z}'_j, \mathbf{z}'_{j'}) - \frac{2}{nm} \sum_{i,j} k(\mathbf{z}_i, \mathbf{z}'_j)$. Both quantities are evaluated on CLIP embeddings; smaller values indicate that \mathcal{D}_{OOD} is closer to the ID manifold.

Class-aware distances. For ID class $c \in \{1, \dots, K\}$, define the (normalized) image-prototype $\boldsymbol{\mu}_c = (\frac{1}{|\mathcal{D}_c|} \sum_{i:y_i=c} \mathbf{z}_i) / \|\frac{1}{|\mathcal{D}_c|} \sum_{i:y_i=c} \mathbf{z}_i\|_2$ and the (normalized) text prototype $\mathbf{t}_c =$

Table 3. OOD Detection methods baselines and variations. This table synthesizes multiple variations using our proposed Projection Filtering approach for all the OOD detection methods considered in this work.

Score	Unmodified	Global	Class	Class Pred	Class Avg
CTM	$\max_k \sin(\mathbf{w}_k, \mathbf{h})$	$\max_k \sin(\mathbf{w}_k, \hat{\mathbf{h}})$	$\max_k \sin(\mathbf{w}_k, \hat{\mathbf{h}}^k)$	$\max_k \sin(\mathbf{w}_k, \hat{\mathbf{h}}^{\text{pred}})$	$\max_k \sin(\mathbf{w}_k, \hat{\mathbf{h}}^{\text{avg}})$
CTM(mean)	$\max_k \sin(\boldsymbol{\mu}_k, \mathbf{h})$	$\max_k \sin(\boldsymbol{\mu}_k, \hat{\mathbf{h}})$	$\max_k \sin(\boldsymbol{\mu}_k, \hat{\mathbf{h}}^k)$	$\max_k \sin(\boldsymbol{\mu}_k, \hat{\mathbf{h}}^{\text{pred}})$	$\max_k \sin(\boldsymbol{\mu}_k, \hat{\mathbf{h}}^{\text{avg}})$
Energy	$-T \log \sum_{k=1}^C e^{g(\mathbf{h})_k/T}$	$-T \log \sum_{k=1}^C e^{g(\mathbf{h})_k/T}$	$-T \log \sum_{k=1}^C e^{\theta_k}$	$-T \log \sum_{k=1}^C e^{g(\hat{\mathbf{h}}^{\text{avg}})_k/T}$	$-T \log \sum_{k=1}^C e^{g(\hat{\mathbf{h}}^{\text{avg}})_k/T}$
MSR	$\max_k \mathbf{p}_k$	$\max_k \hat{\mathbf{p}}_k$	$\max_k \hat{\mathbf{p}}_{\text{class}}$	$\max_k \hat{\mathbf{p}}_{\text{pred}}$	$\max_k \hat{\mathbf{p}}_{\text{avg}}$
MLS	$\max_k g(\mathbf{h})_k$	$\max_k g(\hat{\mathbf{h}})$	$\max_k g(\hat{\mathbf{h}}^{\text{class}})$	$\max_k g(\hat{\mathbf{h}}^{\text{pred}})$	$\max_k g(\hat{\mathbf{h}}^{\text{avg}})$
PE	$\sum_{k=1}^C \mathbf{p}_k \log \mathbf{p}_k$	$\sum_{k=1}^C \hat{\mathbf{p}}_k \log \hat{\mathbf{p}}_k$	$\sum_{k=1}^C (\hat{\mathbf{p}}_{\text{class}}) \log (\hat{\mathbf{p}}_{\text{class}})$	$\sum_{k=1}^C (\hat{\mathbf{p}}_{\text{pred}}) \log (\hat{\mathbf{p}}_{\text{pred}})$	$\sum_{k=1}^C (\hat{\mathbf{p}}_{\text{avg}}) \log (\hat{\mathbf{p}}_{\text{avg}})$
GEN	$\sum_{k=1}^M \mathbf{p}_k^\gamma (1 - \mathbf{p}_k^\gamma)$	$\sum_{k=1}^M \hat{\mathbf{p}}_k^\gamma (1 - \hat{\mathbf{p}}_k^\gamma)$	$\sum_{k=1}^M (\hat{\mathbf{p}}_{\text{class}})^\gamma [1 - (\hat{\mathbf{p}}_{\text{class}})^\gamma]$	$\sum_{k=1}^M (\hat{\mathbf{p}}_{\text{pred}})^\gamma [1 - (\hat{\mathbf{p}}_{\text{pred}})^\gamma]$	$\sum_{k=1}^M (\hat{\mathbf{p}}_{\text{avg}})^\gamma [1 - (\hat{\mathbf{p}}_{\text{avg}})^\gamma]$
REN	$\frac{1}{1-\gamma} \log \sum_{k=1}^M \mathbf{p}_k^\gamma$	$\frac{1}{1-\gamma} \log \sum_{k=1}^M \hat{\mathbf{p}}_k^\gamma$	$\frac{1}{1-\gamma} \log \sum_{k=1}^M (\hat{\mathbf{p}}_{\text{class}})^\gamma$	$\frac{1}{1-\gamma} \log \sum_{k=1}^M (\hat{\mathbf{p}}_{\text{pred}})^\gamma$	$\frac{1}{1-\gamma} \log \sum_{k=1}^M (\hat{\mathbf{p}}_{\text{avg}})^\gamma$
GE	$\sum_{k=1}^C k \mathbf{p}(k)$	$\sum_{k=1}^C k \hat{\mathbf{p}}(k)$	$\sum_{k=1}^C k \hat{\mathbf{p}}_{\text{class}}$	$\sum_{k=1}^C k \hat{\mathbf{p}}_{\text{pred}}$	$\sum_{k=1}^C k \hat{\mathbf{p}}_{\text{avg}}$
PCF	$-\log \sum_{k=1}^C \mathbf{p}_k^2$	$-\log \sum_{k=1}^C \hat{\mathbf{p}}_k^2$	$-\log \sum_{k=1}^C (\hat{\mathbf{p}}_{\text{class}}^{\text{pred}})^2$	$-\log \sum_{k=1}^C (\hat{\mathbf{p}}_{\text{pred}}^{\text{pred}})^2$	$-\log \sum_{k=1}^C (\hat{\mathbf{p}}_{\text{avg}}^{\text{pred}})^2$
Maha	$\max_k \bar{\mathbf{h}}_k^\top \Sigma^{-1} \bar{\mathbf{h}}_k$	$\max_k \bar{\mathbf{h}}_k^\top \bar{\Sigma}^{-1} \bar{\mathbf{h}}_k$	$\max_k (\bar{\mathbf{h}}_k^{\text{pred}})^\top (\bar{\Sigma}^{\text{pred}})^{-1} (\bar{\mathbf{h}}_k^{\text{pred}})$	$\max_k (\bar{\mathbf{h}}_k^{\text{avg}})^\top (\bar{\Sigma}^{\text{avg}})^{-1} (\bar{\mathbf{h}}_k^{\text{avg}})$	
NNguide	$E(\mathbf{h})G(\mathbf{h})$	$E(\hat{\mathbf{h}})G(\hat{\mathbf{h}})$	$E(\mathbf{h}^{\text{pred}})G(\mathbf{h}^{\text{pred}})$	$E(\mathbf{h}^{\text{avg}})G(\mathbf{h}^{\text{avg}})$	
fDBD	$\frac{1}{C-1} \sum_{k \neq m(\mathbf{x})}^C \frac{D_{\text{a}}(\mathbf{h}, k)}{\ \mathbf{h} - \boldsymbol{\mu}_{\text{mean}}\ }$	$\frac{1}{C-1} \sum_{k \neq m(\mathbf{x})}^C \frac{D_{\text{a}}(\hat{\mathbf{h}}, k)}{\ \hat{\mathbf{h}} - \hat{\boldsymbol{\mu}}_{\text{mean}}\ }$	$\frac{1}{C-1} \sum_{k \neq m(\mathbf{x})}^C \frac{D_{\text{a}}(\hat{\mathbf{h}}^{\text{pred}}, k)}{\ \hat{\mathbf{h}}^{\text{pred}} - \hat{\boldsymbol{\mu}}_{\text{pred}}\ }$	$\frac{1}{C-1} \sum_{k \neq m(\mathbf{x})}^C \frac{D_{\text{a}}(\hat{\mathbf{h}}^{\text{avg}}, k)}{\ \hat{\mathbf{h}}^{\text{avg}} - \hat{\boldsymbol{\mu}}_{\text{avg}}\ }$	
pNML	$\log \sum_{k=1}^C \frac{\mathbf{p}_k}{\mathbf{p}_k + \mathbf{p}_k^{\text{avg}} \mathbf{g}(1 - \mathbf{p}_k)}$	$\log \sum_{k=1}^C \frac{\hat{\mathbf{p}}_k}{\hat{\mathbf{p}}_k + \hat{\mathbf{p}}_k^{\text{avg}} \mathbf{g}(1 - \hat{\mathbf{p}}_k)}$	$\log \sum_{k=1}^C \frac{\hat{\mathbf{p}}_k^{\text{pred}}}{\hat{\mathbf{p}}_k^{\text{pred}} + (\hat{\mathbf{p}}_k^{\text{pred}})^{\text{avg}} \mathbf{g}(1 - \hat{\mathbf{p}}_k^{\text{pred}})}$	$\log \sum_{k=1}^C \frac{\hat{\mathbf{p}}_k^{\text{avg}}}{\hat{\mathbf{p}}_k^{\text{avg}} + (\hat{\mathbf{p}}_k^{\text{avg}})^{\text{pred}} \mathbf{g}(1 - \hat{\mathbf{p}}_k^{\text{avg}})}$	
GradNorm	$\left\ \frac{1}{C} \sum_{k=1}^C \frac{\partial \mathcal{L}_{\text{CE}}(g(\mathbf{h}), k)}{\partial \mathbf{w}} \right\ $	$\left\ \frac{1}{C} \sum_{k=1}^C \frac{\partial \mathcal{L}_{\text{CE}}(g(\hat{\mathbf{h}}^{\text{pred}}), k)}{\partial \mathbf{w}} \right\ $	$\left\ \frac{1}{C} \sum_{k=1}^C \frac{\partial \mathcal{L}_{\text{CE}}(g(\hat{\mathbf{h}}^{\text{avg}}), k)}{\partial \mathbf{w}} \right\ $	$\left\ \frac{1}{C} \sum_{k=1}^C \frac{\partial \mathcal{L}_{\text{CE}}(g(\hat{\mathbf{h}}^{\text{avg}}), k)}{\partial \mathbf{w}} \right\ $	
PCA Error			$\max_k - \frac{\ \mathbf{h} - \mathbf{h}_k\ }{\ \mathbf{h}\ }$	$\max_k - \frac{\ \mathbf{h} - \mathbf{h}_k^{\text{pred}}\ }{\ \mathbf{h}\ }$	$\max_k - \frac{\ \mathbf{h} - \mathbf{h}_k^{\text{avg}}\ }{\ \mathbf{h}\ }$
VIM	$\alpha \ \hat{\mathbf{R}}\mathbf{h}\ + E(\mathbf{h})$				
NeCo		$\frac{\ \hat{P}\mathbf{h}\ }{\ \mathbf{h}\ }$			
Residual		$\ \hat{\mathbf{R}}\mathbf{h}\ $			
Confidence		$s_{\mathbf{W}}$			

$(\frac{1}{L} \sum_{\ell=1}^L \phi_{\text{text}}(\text{prompt}_{\ell}(c))) / \left\| \frac{1}{L} \sum_{\ell=1}^L \phi_{\text{text}}(\text{prompt}_{\ell}(c)) \right\|_2$ (using prompt ensembling for class c). For a test embedding \mathbf{z}' , define the nearest-centroid cosine distance $d_{\text{NC}}(\mathbf{z}') = 1 - \max_{c \leq K} \mathbf{z}'^{\top} \boldsymbol{\mu}_c$, and the image–text cosine distance $d_{\text{IT}}(\mathbf{z}') = 1 - \max_{c \leq K} \mathbf{z}'^{\top} \mathbf{t}_c$. Aggregate per-dataset by averaging: $\bar{d}_{\text{NC}} = \frac{1}{m} \sum_{j=1}^m d_{\text{NC}}(\mathbf{z}'_j)$ and $\bar{d}_{\text{IT}} = \frac{1}{m} \sum_{j=1}^m d_{\text{IT}}(\mathbf{z}'_j)$. Lower values mean the OOD set is *class-closer* to ID.

Clustering into proximity buckets. We orient all four metrics so that lower \Rightarrow closer and form a feature vector $\mathbf{v}(D_{\text{OOD}}) = [\text{FD}^2, \widehat{\text{MMD}}^2, \bar{d}_{\text{NC}}, \bar{d}_{\text{IT}}]^{\top}$. We standardize \mathbf{v} across candidate OOD sets (z-score per coordinate) and run k -means with $k = 3$ (fixed seed) to obtain proximity buckets labeled *near/mid/far*. This CLIP-based protocol is detector-agnostic and applies unchanged to any ID label space or downstream OOD scoring rule.

C. Statistical Tests for Clique Generation

Let k be the number of CSFs and N the number of complete blocks (e.g., each block is a dataset/condition on which all k methods are evaluated on the same metric). Within block $i \in \{1, \dots, N\}$, rank the methods so that $r_{ij} \in \{1, \dots, k\}$ is the rank of method j (use mid-ranks for ties). Define the average rank $\bar{R}_j = \frac{1}{N} \sum_{i=1}^N r_{ij}$. The Friedman statistic tests the null H_0 : all methods are equivalent in distribution of ranks (Fréchet, 1957; Demšar, 2006):

$$Q = \frac{12N}{k(k+1)} \sum_{j=1}^k \bar{R}_j^2 - 3N(k+1),$$

(optionally applying a standard tie correction within blocks). For finite samples, the Iman–Davenport F -approximation is recommended (Iman & Davenport, 1980):

$$F_F = \frac{(N-1)Q}{N(k-1) - Q} \sim F_{k-1, (k-1)(N-1)}.$$

If F_F exceeds the critical value at level α , we reject H_0 and proceed with post-hoc pairwise comparisons.

Conover post-hoc & Bron–Kerbosch cliques (top groups). For each pair (i, j) we compare average ranks using Conover’s post-hoc test (Conover, 1999). With common standard error

$$\text{SE} = \sqrt{\frac{k(k+1)}{6N}}, \quad T_{ij} = \frac{|\bar{R}_i - \bar{R}_j|}{\text{SE}},$$

two-sided p -values are obtained from the normal (or t) reference, and multiplicity is controlled across all $\binom{k}{2}$ pairs using Holm’s step-down procedure (Holm, 1979). To summarize statistically indistinguishable winners, construct an *indifference graph* $G = (V, E)$ with nodes $V = \{1, \dots, k\}$ (methods) and edges $(i, j) \in E$ iff the adjusted $p_{ij} \geq \alpha$ (i.e., the pair is not significantly different). Enumerate all *maximal cliques* of G using the Bron–Kerbosch algorithm with pivoting (state (R, P, X) ; recursively add $v \in P \setminus N(u)$ for a high-degree pivot u ; output R when $P = X = \emptyset$) (Bron & Kerbosch, 1973). Each maximal clique is a set of methods that are mutually indistinguishable under Conover–Holm; reporting the leading clique(s), sorted by best/mean \bar{R} , yields layered, statistically justified “top groups,” alongside \bar{R}_j and the full adjusted p -matrix for transparency.

C.1. Simplified example

To illustrate the evaluation methodology, we consider a simplified scenario involving $k = 6$ Confidence Scoring Functions (CSFs): Confidence, GEN, MSR, CTM, fDBD, and Energy. We evaluate these models on the CIFAR-10 dataset using the AUGRC metric, focusing solely on the misclassification scenario. The evaluation aggregates results across three training paradigms, each executed five times, resulting in a total of $N = 15$ experimental blocks.

As shown in Table 5a, within each block (characterized by a unique combination of dataset, paradigm, metric, and run), the CSFs are ranked based on their performance scores. Lower ranks indicate superior performance. These rankings are then averaged across all $N = 15$ blocks, as summarized in Table 5b.

Using these average ranks, we compute the Friedman statistic, yielding $F_F = 46.162$ with a p -value = 8.418×10^{-9} . Since this p -value falls below the significance level $\alpha = 0.05$, we reject the null hypothesis and conclude that significant differences exist between the CSFs. Consequently, we proceed with post-hoc pairwise comparisons.

(a) CLIP-based distance metrics. Dataset: CIFAR-10

		Global		Class-aware		Group
		Kernel MMD	FD	Label-Text Alignment	Image Centroid Distance	
Test	-0.0000	0.0028	0.7183	0.6349	ID	
CIFAR-100	0.0002	0.1592	0.7885	0.8085	Near	
TinyImagenet	0.0009	0.3233	0.8060	0.9256	Near	
iSUN	0.0015	0.4890	0.7943	0.8393	Mid	
LSUN resize	0.0016	0.5248	0.8045	0.8634	Mid	
LSUN cropped	0.0015	0.5129	0.7797	0.8168	Mid	
SVHN	0.0020	0.7009	0.7744	0.8607	Mid	
Places 365	0.0021	0.6379	0.8337	1.1471	Far	
Textures	0.0020	0.6698	0.8231	1.0647	Far	

(b) CLIP-based distance metrics. Dataset: SuperCIFAR-100

		Global		Class-aware		Group
		Kernel MMD	FD	Label-Text Alignment	Image Centroid Distance	
Test	0.0000	0.0748	0.7581	0.7031	ID	
CIFAR-10	0.0002	0.1705	0.7701	0.7511	Near	
TinyImagenet	0.0008	0.2307	0.7840	0.8738	Near	
iSUN	0.0012	0.3856	0.7607	0.7425	Mid	
LSUN resize	0.0013	0.4244	0.7625	0.7720	Mid	
LSUN cropped	0.0011	0.3999	0.7695	0.7351	Mid	
SVHN	0.0017	0.6208	0.7566	0.8012	Mid	
Places 365	0.0020	0.5562	0.7939	1.0964	Far	
Textures	0.0016	0.5246	0.7980	1.0003	Far	

(c) CLIP-based distance metrics. Dataset: CIFAR-100

		Global		Class-aware		Group
		Kernel MMD	FD	Label-Text Alignment	Image Centroid Distance	
Test	-0.0000	0.0033	0.7043	0.6026	ID	
CIFAR-10	0.0002	0.1590	0.7494	0.7268	Near	
TinyImagenet	0.0008	0.2235	0.7512	0.8436	Near	
iSUN	0.0012	0.3829	0.7484	0.7128	Mid	
LSUN resize	0.0013	0.4204	0.7562	0.7388	Mid	
LSUN cropped	0.0011	0.3999	0.7364	0.7120	Mid	
SVHN	0.0017	0.6222	0.7511	0.7789	Mid	
Places 365	0.0019	0.5456	0.7752	1.0568	Far	
Textures	0.0016	0.5232	0.7613	0.9780	Far	

Table 5. Friedman test across entities with blocks.

(a) Block example							(b) Averaged rankings	
Dataset	Paradigm	Metric	Run	CSF	Score	Rank	CSF	Avg Rank
test	confidnet	AUGRC	1	Confidence	4.453	0.17	GEN	0.278
test	confidnet	AUGRC	1	GEN	4.619	0.33	Confidence	0.367
test	confidnet	AUGRC	1	MSR	4.737	0.50	MSR	0.511
test	confidnet	AUGRC	1	CTM	5.479	0.67	CTM	0.656
test	confidnet	AUGRC	1	fDBD	5.677	0.83	fDBD	0.767
test	confidnet	AUGRC	1	Energy	5.811	1.0	Energy	0.922

We apply Conover's post-hoc test to compare the average rankings, computing two-sided p -values with controlled multiplicity via Holm's step-down procedure (Holm, 1979) (see Figure 2). This analysis allows us to identify "cliques" or groups of CSFs that are statistically indistinguishable from one another ($p_{ij} \geq 0.05$). In this example, we identify five cliques: Clique 1: ['CTM', 'MSR'], Clique 2: ['CTM', 'fDBD'], Clique 3: ['Confidence', 'GEN'], Clique 4: ['Confidence', 'MSR'], and Clique 5: ['Energy'].

While visual identification of cliques is straightforward in this small-scale example, the combinatorial complexity increases significantly with a larger number of CSFs. To address this, we employ the Bron-Kerbosch algorithm to systematically identify maximal cliques in larger scenarios. Once identified, the cliques are ranked based on their constituent members. Finally, we select non-overlapping cliques using a greedy layering approach, organizing them from best to worst performance. The resulting hierarchical layers are presented in Table 6. For Figure 1, we only report the first layer for all the possible scenarios.

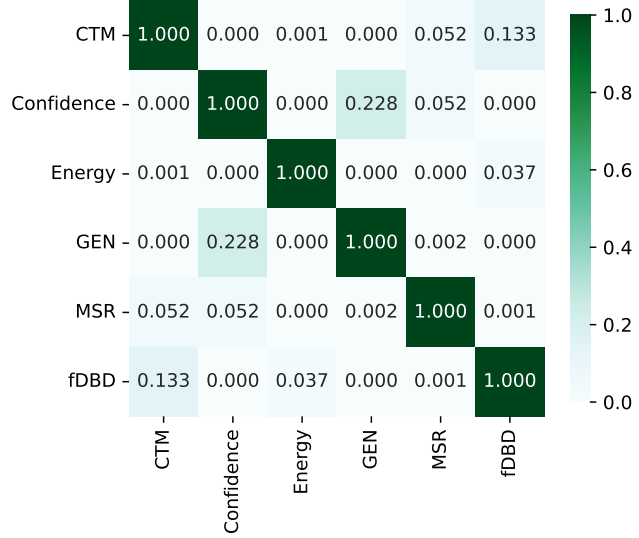

Figure 2. Conover-Holm p -values

Table 6. Layered cliques ranked from best to worst

Layer	Average Rank	Members
1	1.933	Confidence, GEN
2	3.500	CTM, MSR
3	5.533	Energy

D. Neural-Collapse-based Analysis

We provide a geometric interpretation of our empirical findings through the lens of Neural Collapse (NC), focusing on the last-layer feature space and classifier geometry. Taking into consideration the Definitions and Notations in Section 3.1, we quantify proximity to NC using the metrics described by (Papyan et al., 2020):

- **Equinormness of the class means** ($\|\boldsymbol{\mu}_i\| = \|\boldsymbol{\mu}_j\|$): $\frac{\text{Std}_c(\|\tilde{\boldsymbol{\mu}}_c\|_2)}{\text{Avg}_c(\|\tilde{\boldsymbol{\mu}}_c\|_2)}$
- **Equinormness of the classifier weights** ($\|\mathbf{w}_i\| = \|\mathbf{w}_j\|$): $\frac{\text{Std}_c(\|\mathbf{w}_c\|_2)}{\text{Avg}_c(\|\mathbf{w}_c\|_2)}$
- **Equiangularity of the class means** ($\cos_{\boldsymbol{\mu}}(i, j) = \beta$): $\text{Std}_{c, c' \neq c}(\cos_{\boldsymbol{\mu}}(c, c'))$
- **Equiangularity of the classifier weights** ($\cos_{\mathbf{w}}(i, j) = \rho$): $\text{Std}_{c, c' \neq c}(\cos_{\mathbf{w}}(c, c'))$
- **Maximal Equiangularity of the class means** ($\cos_{\boldsymbol{\mu}}(i, j) = -\frac{1}{C-1}$): $\text{Avg}_{c, c'}|\cos_{\boldsymbol{\mu}}(c, c') + \frac{1}{C-1}|$
- **Maximal Equiangularity of the classifier weights** ($\cos_{\mathbf{w}}(i, j) = -\frac{1}{C-1}$): $\text{Avg}_{c, c'}|\cos_{\mathbf{w}}(c, c') + \frac{1}{C-1}|$
- **Within-class variation collapse** ($\mathbf{h} \rightarrow \boldsymbol{\mu}_k$): $\text{Tr}\left(\frac{\boldsymbol{\Sigma}_{\mathbf{W}} \boldsymbol{\Sigma}_{\mathbf{B}}^{\dagger}}{C}\right)$
- **Self-duality** ($\mathbf{w}_k = \alpha \boldsymbol{\mu}_k$): $\left\| \left(\frac{\mathbf{W}}{\|\mathbf{W}\|_F} \right)^T - \frac{\mathbf{M}}{\|\mathbf{M}\|_F} \right\|_F^2 = \left\| \frac{1}{\|\mathbf{W}\|_F} \mathbf{W}^T - \frac{1}{\|\mathbf{M}\|_F} \mathbf{M} \right\|_F^2 = \left\| \frac{1}{\|\mathbf{W}\|_F} \mathbf{W}^T \right\|_F^2 + \left\| \frac{1}{\|\mathbf{M}\|_F} \mathbf{M} \right\|_F^2 - 2 \frac{\text{Tr}(\mathbf{W}\mathbf{M})}{\|\mathbf{W}\|_F \|\mathbf{M}\|_F} = 2 - 2 \frac{\text{Tr}(\mathbf{W}\mathbf{M})}{\|\mathbf{W}\|_F \|\mathbf{M}\|_F}$

where $\tilde{\boldsymbol{\mu}}_c = \boldsymbol{\mu}_c - \boldsymbol{\mu}$ is the class-centered mean, $\cos_{\boldsymbol{\mu}}(c, c') = \frac{\tilde{\boldsymbol{\mu}}_c^T \tilde{\boldsymbol{\mu}}_{c'}}{\|\tilde{\boldsymbol{\mu}}_c\|_2 \|\tilde{\boldsymbol{\mu}}_{c'}\|_2}$ is cosine similarity between any pair of class-centered means c and c' , $\cos_{\mathbf{w}}(c, c') = \frac{\mathbf{w}_c^T \mathbf{w}_{c'}}{\|\mathbf{w}_c\|_2 \|\mathbf{w}_{c'}\|_2}$ is cosine similarity between any pair of classifier weights c and c' , $\boldsymbol{\Sigma}_{\mathbf{W}} = \text{Avg}_{i, c}(\mathbf{h}_{i, c} - \boldsymbol{\mu})(\mathbf{h}_{i, c} - \boldsymbol{\mu})^T$ is the within-class covariance, $\boldsymbol{\Sigma}_{\mathbf{B}} = \text{Avg}_c(\tilde{\boldsymbol{\mu}}_c \tilde{\boldsymbol{\mu}}_c^T)$ is the between-class covariance, \dagger is the Moore-Penrose pseudoinverse, and $\mathbf{M} = [\tilde{\boldsymbol{\mu}}_c : c = 1, \dots, C]$ is the centered class-mean matrix.

We compute these metrics for each model and dataset under three activation regimes: unfiltered, global PCA projection filtering, and class-predicted PCA projection filtering, and interpret how shifts in these metrics align with shifts in the relative performance of confidence scoring functions. Tables 7a and 7b show the NC metrics for all the activation regimes, considering CNN and ViT models respectively, and Table 7c contains the NC metrics associated to the classifier weights and.

D.1. CNNs trained from scratch (VGG-13)

D.1.1. WHY IS CTM THE DETECTION METHOD THAT PERFORMS THE BEST WHEN THE MODEL HAS BEEN TRAINED ON TINYIMAGENET USING CNNS?

As Table 7a shows, Maximal Equiangularity, Variability Collapse, and Self Duality are the strongest NC metrics when TinyImageNet is used to train the VGG-13 models, while Equinormness and Equiangularity are the weakest. In these conditions prototype-alignment becomes highly reliable, which can be exploited by the CTM score. When Self-Duality occurs the classifiers align with the class means up to a scalar : $\mathbf{W} \propto \mathbf{M}^T \implies \mathbf{w}_c = \alpha \boldsymbol{\mu}_c$, then $\text{CTM}(\mathbf{x}) = \max_k \text{sim}(\mathbf{w}_k, \mathbf{h}) = \max_k \frac{\mathbf{w}_k^T \mathbf{h}}{\|\mathbf{w}_k\|_2 \|\mathbf{h}\|_2} = \max_k \frac{\alpha \boldsymbol{\mu}_k^T \mathbf{h}}{\|\alpha \boldsymbol{\mu}_k\|_2 \|\mathbf{h}\|_2}$. If Variability Collapse is achieved $\boldsymbol{\Sigma}_{\mathbf{W}} \rightarrow 0$, meaning features \mathbf{x} collapse to their class means $\boldsymbol{\mu}_k$: $\mathbf{h} \rightarrow \boldsymbol{\mu}_k$. Therefore, $\text{CTM}(\mathbf{x}) = \max_k \frac{\boldsymbol{\mu}_k^T \mathbf{h}}{\|\boldsymbol{\mu}_k\|_2 \|\mathbf{h}\|_2} \approx \frac{\boldsymbol{\mu}_k^T \boldsymbol{\mu}_k}{\|\boldsymbol{\mu}_k\|_2 \|\boldsymbol{\mu}_k\|_2} = 1$, which creates a deterministic score for ID samples. Even if Equiangularity is not achieved completely (meaning the gap between Class A and Class B is different from Class A and Class C), the CTM score for an ID input is approximately 1. In the other hand, Maximal Angular Margin dictates that class means form a Simplex ETF, maximizing the separation angle θ_{ij} between any distinct classes i, j : $\cos(\boldsymbol{\mu}_i, \boldsymbol{\mu}_j) = -\frac{1}{K-1} \quad \forall i \neq j$. This implies that the collapsed ID feature space is maximally sparse in terms of angular distribution. For an OOD sample \mathbf{x}^{OOD} lying in the subspace orthogonal to the ID manifold (or between vertices), the maximum cosine similarity is bounded by the geometry of the simplex. Unlike dense feature spaces where an OOD point might accidentally align with a cluster, the ETF geometry ensures wide angular gaps (negative

Table 7. Neural Collapse metrics

(a) NC metrics for VGG-13 models.

Dataset	Projection	EqNorm	EqAng	max-EqAng	Var Collapse	Self Duality
CIFAR-10	None	0.0266	0.0651	0.2447	0.0081	0.0320
	Global	0.0266	0.0651	0.2447	0.0082	0.0307
	Class pred	0.0268	0.0650	0.2447	0.0080	0.0320
SuperCIFAR-100	None	0.0246	0.0678	0.1537	0.0095	0.0519
	Global	0.0246	0.0679	0.1537	0.0095	0.0507
	Class pred	0.0248	0.0678	0.1537	0.0093	0.0519
CIFAR-100	None	0.0743	0.1049	0.0950	0.0079	0.1279
	Global	0.0745	0.1052	0.0952	0.0259	0.1232
	Class pred	0.0743	0.1049	0.0950	0.0069	0.1278
TiinyImageNet	None	0.0544	0.0900	0.0761	0.0021	0.0322
	Global	0.0546	0.0903	0.0763	0.0044	0.0335
	Class pred	0.0546	0.0901	0.0762	0.0016	0.0322

(b) NC metrics for ViT models.

Dataset	Projection	EqNorm	EqAng	max-EqAng	Var Collapse	Self Duality
CIFAR-10	None	0.0869	0.2505	0.3770	0.0120	1.2692
	Global	0.0870	0.2505	0.3771	0.0120	1.2716
	Class pred	0.0870	0.2505	0.3770	0.0120	1.2693
SuperCIFAR-100	None	0.1432	0.2403	0.2814	0.0152	1.0922
	Global	0.1432	0.2403	0.2814	0.0153	1.0937
	Class pred	0.1435	0.2406	0.2816	0.0150	1.0929
CIFAR-100	None	0.1054	0.1322	0.1172	0.0124	0.8535
	Global	0.1058	0.1328	0.1177	0.0162	0.8566
	Class pred	0.1065	0.1327	0.1177	0.0107	0.8548
TiinyImageNet	None	0.1950	0.1984	0.1647	0.0372	1.1292
	Global	0.1971	0.2008	0.1665	0.0806	1.1429
	Class pred	0.2069	0.2066	0.1716	0.0289	1.1416

(c) NC metrics for classifier weights \mathbf{w} .

Model	Dataset	EqNorm	EqAng	max-EqAng
VGG-13	CIFAR-10	0.0143	0.0707	0.2455
	SuperCIFAR-100	0.0184	0.0529	0.1414
	CIFAR-100	0.0730	0.0611	0.0665
	TiinyImageNet	0.0250	0.0748	0.0666
ViT	CIFAR-10	0.0141	0.0372	0.2884
	SuperCIFAR-100	0.0217	0.0360	0.1526
	CIFAR-100	0.0274	0.0450	0.0551
	TiinyImageNet	0.0178	0.0364	0.0390

correlations) between prototypes, statistically minimizing $\max_k \cos(\mathbf{w}_k, \mathbf{h})$. OOD samples, which lie in the angular gaps, will strictly have scores < 1 as long as Maximal Angularity holds (the vectors point in distinct directions). CTM measures alignment with prototype: $\mathbf{h}^{\text{OOD}} \in \text{Null Space} \implies \cos(\boldsymbol{\mu}_k, \mathbf{h}^{\text{OOD}}) \approx 0$. An OOD sample cannot be perfectly parallel to any prototype, so $\cos(\boldsymbol{\mu}_k, \mathbf{h}^{\text{OOD}}) \ll 1$. In summary, CTM strips away the noise of magnitude (Equinorm failure) and relies on the purity of direction (Maximal Angularity) and clustering (Variability Collapse).

D.1.2. WHY ENERGY, MLS AND NNGUIDE DETECTION METHODS PERFORM THE BEST WHEN THE MODEL HAS BEEN TRAINED ON CIFAR-10 AND SUPERCIFAR-100 USING CNNs?

In the context of CIFAR-10, Equinormness, Equiangularity, Variability Collapse, and Self-Duality emerge as the most robust metrics, whereas Maximal Equiangularity demonstrates the least adherence to a collapsed regime, as Table 7a exhibits. SuperCIFAR-100 shows a similar metrics profile to CIFAR-10 with an improved Maximal Equiangularity, but slight deterioration in Self-Duality. In both NC regimes, logit-derived scores such as Energy and MLS benefit from stable, class-unbiased logit scaling induced by Equinormness and the differentiated target vs. non-target angular margin implied by Equiangular geometry. More specifically, Self-Duality implies the classifiers weights \mathbf{W} align with the class means \mathbf{M} up to a scalar α : $\mathbf{W} \propto \mathbf{M}^\top \implies \mathbf{w}_c = \alpha \boldsymbol{\mu}_c$ and Equinorm states that any pair of class means c and c' have equal ℓ_2 norm: $\|\boldsymbol{\mu}_c\|_2 = \|\boldsymbol{\mu}_{c'}\|_2 = R$. Substituting these into the logit $g(\mathbf{h})_k$ for a correctly classified ID sample (target logit) $\mathbf{h} \rightarrow \boldsymbol{\mu}_c$: $g(\mathbf{h})_k = \mathbf{w}_k^\top \mathbf{h} + b_k \approx \mathbf{w}_k^\top \boldsymbol{\mu}_k = \alpha \|\boldsymbol{\mu}_k\|^2 = \alpha R^2$. Thus, the minimum possible energy for ID data is uniform across all classes: $\text{Energy}(\mathbf{x}) \approx -\alpha R^2$. This uniformity prevents class-conditional bias, where some ID classes might otherwise have naturally higher energy (and thus higher False Positive Rates) than others due to varying feature norms. Equiangularity dictates that any pair of class means are equally spaced $\cos(\boldsymbol{\mu}_i, \boldsymbol{\mu}_j) = \beta, \forall i \neq j$, meaning that for an off-target logit $g(\mathbf{h})_j = \mathbf{w}_j^\top \mathbf{h} + b_k \approx \mathbf{w}_j^\top \boldsymbol{\mu}_k = \alpha \|\boldsymbol{\mu}_k\|^2 \beta = \alpha R^2 \beta$.

Let's analyze the behavior of the detection scores under these conditions. The Energy score sums over the exponentiated logits $\sum e^{g(\mathbf{h})_k} = e^{\alpha R^2} + (K-1)e^{\alpha R^2 \beta}$, which in the optimal case (Maximal Equiangularity $\beta = -\frac{1}{C-1}$) would be dominated by $e^{\alpha R^2}$ since $e^{\alpha R^2} \gg (C-1)e^{\alpha R^2 \beta}$ or $\alpha R^2 > \frac{\ln(C-1)}{1-\beta}$. This last expression reveals that β allows some tolerance to make the target logit distinguishable from the off-target logits as $\beta < 1 - \frac{\ln(C-1)}{\alpha R^2}$ when evaluating ID inputs. This explains why the Energy score is still very effective at detecting OOD inputs in this scenario where Maximal Equiangularity is not the strongest. However, the failure mode for this score occurs when either the OOD sample falls in the geometric of a cluster that aligns with all C classes, provoking an artificially high score, or when the norm for an OOD sample is anomalously large. The poor performance of the Energy score in far OOD scenarios seems to indicate that the latter is the problem, which can be validated by the performance of MLS. The MLS score, unlike the Energy score, ignores off-target logits entirely since $\text{MLS}(\mathbf{x}) = \max_{k \leq C} g(\mathbf{h})_k$. Thus, as long as the classes are distinct ($\beta < 1$), the target logit is strictly greater than the non-target logits given that $\text{MLS}(\mathbf{x}) = \max(\alpha R^2, \alpha R^2 \beta)$. Assuming that the class means are not clustered together, the failure mode of MLS lies on its dependence on feature magnitude. Given the similar performance of the Energy score and MLS when CIFAR-10 is the training set, we argue that OOD norms can be differentiated from ID norms in this case. Model trained SuperCIFAR-100, in the other hand, seems to be more vulnerable to atypical large norms, specially when far OOD datasets are tested.

D.1.3. WHY NNGUIDE PERFORMS WELL WHEN THE MODEL HAS BEEN TRAINED ON CIFAR-10 USING CNNs?

NNGuide acts as a confidence-weighted geometric filter that corrects the summation bias inherent in the Energy score when classes are clustered (non-maximal equiangularity). In this regime, the Energy score could become unreliable because the summation aggregates multiple medium-strength logits from clustered classes. If an OOD sample lies in the geometric center of a cluster with cosine similarity $\beta > 0$, it activates all K classifiers moderately, resulting in a partition sum that can rival the single high-confidence logit of an ID sample, leading to false positives. NNGuide modulates this by multiplying the base score with a guidance term $G(\mathbf{h})$, computed from the k nearest training neighbors: $\text{NNGuide}(\mathbf{x}) = S_{\text{base}}(\mathbf{h}) \cdot G(\mathbf{h}) = S_{\text{base}}(\mathbf{h}) \cdot \left(\frac{1}{k} \sum_{i=1}^k S_{\text{base}}(\mathbf{h}_{(i)}) \cdot \cos(\mathbf{h}, \mathbf{h}_{(i)}) \right)$. This term leverages the Self-Duality of Neural Collapse, where the nearest neighbors $\mathbf{h}_{(i)}$ for valid samples are high-confidence prototypes ($S_{\text{base}}(\mathbf{h}_{(i)}) \approx S_{\text{max}}$), effectively turning $G(\mathbf{h})$ into a clean geometric penalty.

NNGuide succeeds in the clustered regime ($\beta > 0$) because the guidance term enforces an angular margin that the raw Energy score ignores. For an ID sample aligned with its class direction, the cosine similarity is near 1, yielding a guidance factor of $G(\mathbf{h}) \approx S_{\text{max}} \cdot 1$. Conversely, for an OOD sample in the angular gap between clustered vectors, the cosine similarity to the nearest neighbors is bounded by the cluster geometry: $G(\mathbf{h}^{\text{OOD}}) \approx S_{\text{max}} \cdot \beta$. Even if the base Energy scores

are indistinguishable ($S_{\text{base}}(\mathbf{h}^{\text{OOD}}) \approx S_{\text{base}}(\mathbf{h})$) due to summation explosion, NNGuide suppresses the OOD score by the factor β : $\frac{\text{NNGuide}(\mathbf{x}^{\text{OOD}})}{\text{NNGuide}(\mathbf{x})} \approx \frac{S_{\text{base}}(\mathbf{h}^{\text{OOD}}) \cdot \beta}{S_{\text{base}}(\mathbf{h}) \cdot 1} = \beta$. As long as the classes are not perfectly overlapping ($\beta < 1$), this multiplicative correction restores the separability that the base score lost. However, NNGuide succumbs to failure modes where this geometric penalty is either insufficient or overridden. The first mode is Tight Clustering ($\beta \rightarrow 1$), where classes become so semantically similar that the angular margin vanishes; here, the penalty factor β approaches 1, rendering the guidance term useless ($G(\mathbf{h}^{\text{OOD}}) \approx G(\mathbf{h})$). The second and more critical failure mode is its sensitivity to feature magnitude. While the guidance term $G(\mathbf{h})$ is scale-invariant (due to cosine normalization), the base term $S_{\text{base}}(\mathbf{h})$ scales linearly with the feature norm $\|\mathbf{h}\|$. If an OOD sample has an anomalously large magnitude where $\|\mathbf{h}^{\text{OOD}}\| = \gamma \|\mathbf{h}\|$ with $\gamma > 1$, the linear growth of the base score overrides the constant geometric penalty: $\text{NNGuide}(\mathbf{x}^{\text{OOD}}) \approx (\gamma S_{\text{base}}) \cdot (S_{\text{max}} \beta)$.

D.1.4. WHY CTMMEAN GLOBAL AND NNGUIDE GLOBAL IMPROVE WITH RESPECT TO THEIR COUNTERPARTS THAT DO NOT USE THE GLOBAL FILTERING FOR MID-OOD DATASETS WHEN USING CNNs?

As Table 7a shows, the NC metrics after Global Projection Filtering do not significantly change for the ID data. Therefore, the improvement in detection cannot be attributed to the ID classes becoming tighter or more separated from each other after filtering. Instead, the improvement comes from how the OOD data is transformed relative to the ID manifold after the projection. Since the improvement occurs for CTMmean and NNGuide, we can attribute it to the angular information as the main reason. Global Projection Filtering acts as a selective denoiser that benefits Mid-OOD detection by severing the shared low-level statistics, like texture or color, that confuse angular detectors. Mid-OOD samples often reside in the same positive feature cone as ID data. The projection operation $\mathbf{P}\mathbf{P}^{\top}(\mathbf{h}^{\text{OOD}} - \boldsymbol{\mu})$ centers the data and removes the low-variance directions responsible for these spurious correlations. By stripping away these common-mode statistics, the projected Mid-OOD vector effectively collapses toward the global mean, becoming angularly ambiguous relative to the distinct class prototypes. This drastically lowers their cosine similarity scores in methods like CTMmean and NNGuide, reducing false positives. In contrast, Far-OOD samples do not benefit from this refinement because they are already geometrically distinct. These samples typically lie in the null space of the ID manifold or are orthogonal to the semantic class directions. Since their angular separation from ID prototypes is already maximized (they look nothing like the training classes), the projection step is redundant. Thus, the projection operation acts as an identity transformation regarding their detectability. However, this projection does not solve the problem of atypically large norms from Far-OOD samples. The principal components \mathbf{P} often capture generic image statistics (e.g., contrast, brightness) shared by all natural images, not just semantic class features. If a Far-OOD sample has an anomalously large norm due to domain shift (e.g., high saturation), its projection onto these generic axes preserves this magnitude: $\|\hat{\mathbf{h}}^{\text{OOD}}\| \leq \|\mathbf{P}\mathbf{P}^{\top}\mathbf{h}^{\text{OOD}}\| + \|(\mathbf{I} - \mathbf{P}\mathbf{P}^{\top})\boldsymbol{\mu}\|$. Consequently, magnitude-sensitive detectors like Energy or MLS can still fail on Far-OOD data if the norm is large enough to override the angular mismatch, necessitating the use of normalized scores like CTM (divides by $\|\mathbf{h}\|$) or fDBD (regularizes by $\|\mathbf{h} - \boldsymbol{\mu}\|$) which are invariant to this preserved scale.

D.1.5. WHY FDBD PERFORMS WELL WHEN THE MODEL HAS BEEN TRAINED ON CIFAR-100 USING CNNs?

The NC metrics for CIFAR-100 report the weakest adherence to a collapsed regime compared to the other datasets, with Maximal Equiangularity for class means and for classifier weights being the strongest metrics. The lack of a strong Variability Collapse, however, makes it difficult for CTM to be competitive in this case. fDBD succeeds because it exploits the rigid geometric skeleton of the classifier weights to create a robust angular detector that is tolerant of feature noise. The fDBD score is defined as the average distance to all non-predicted classes, regularized by the feature distance to the mean of training features: $\text{fDBD}(\mathbf{x}) = \frac{1}{|\mathcal{C}| - 1} \sum_{c \neq f(\mathbf{x})} \frac{D_m(\mathbf{h}, c)}{\|\mathbf{h} - \boldsymbol{\mu}_{\text{train}}\|_2}$, where $D_m(\mathbf{h}, j) = \frac{|(\mathbf{w}_{m(\mathbf{x})} - \mathbf{w}_j)^{\top} \mathbf{h} + (b_{m(\mathbf{x})} - b_j)|}{\|\mathbf{w}_{m(\mathbf{x})} - \mathbf{w}_j\|_2}$. In this regime fDBD outperforms prototype methods because it measures the true safety margin relative to the decision boundary, whereas prototype methods measure centrality relative to a potentially unsafe centroid. The summation of the fDBD score is proportional to the projection of the mean onto the weight difference vectors: $\text{fDBD}(\mathbf{x}) \propto \sum_{j \neq k} (\mathbf{w}_k - \mathbf{w}_j)^{\top} \mathbf{h}$. When Self-Duality fails, the geometric center ($\boldsymbol{\mu}_k$) and the decision center (\mathbf{w}_k) diverge. If $\boldsymbol{\mu}_k$ is close to the boundary (small projection onto $\mathbf{w}_k - \mathbf{w}_j$), fDBD correctly reports a low score, identifying the higher risk of misclassification that CTM would ignore in this scenario. Even with misalignment, Maximal Angularity of \mathbf{W} ensures the decision region is a wide cone supported by the collective opposition of all other classes. Using the ETF property ($\sum_{j \neq k} \mathbf{w}_j = -\mathbf{w}_k$), the fDBD summation simplifies: $\sum_{j \neq k} (\mathbf{w}_k - \mathbf{w}_j)^{\top} \mathbf{h} = (C - 1)\mathbf{w}_k^{\top} \mathbf{h} - (\sum_{j \neq k} \mathbf{w}_j)^{\top} \mathbf{h} = C(\mathbf{w}_k^{\top} \mathbf{h})$. As long as the classifier is accurate (meaning $\mathbf{w}_k^{\top} \mathbf{h} > 0$), the ETF geometry amplifies the margin by a factor of C . fDBD captures this collective margin, ensuring that even a misaligned ID sample is distinguished from OOD samples where $\mathbf{w}_k^{\top} \mathbf{h}^{\text{OOD}} \approx 0$. The

regularization term improves the evaluation when atypically feature norms are atypically large.

D.2. Finetuned Transformers (ViT)

Unlike CNNs trained from scratch, ViTs that were pretrained and finetuned might not have null space for OOD inputs in many cases. Since the ViT networks were pretrained using ImageNet1K, and finetuned using dataset with fewer number of classes, it is likely that the OOD inputs would be projected to existing subspaces that were created during pretraining. This can be corroborated by the NC metrics of ViT models compared to the NC metrics of VGG models. ViT's NC metrics are higher than their CNN's counterparts. This phenomenon has been documented before (Zhou et al., 2025). When the pretraining data has more classes than the finetuning data, then the finetuning process would readjust the boundaries around the classes are the most similar, eg. if the finetuning data contains the class dog, and the pretraining data has classes dog, fox, wolf, and coyotes, then the boundaries after finetuning would enclose all these classes. However when it comes to OOD detection, the strategies cannot rely on the same approaches as models trained from scratch.

D.2.1. WHY THE GLOBAL PROJECTION FILTERING IMPROVES THE OOD SCORES THAT USE ENTROPY OR PROBABILISTIC OUTPUTS WHEN EVALUATING MISCLASSIFICATION FOR ViT MODELS THAT WERE PRETRAINED AND FINETUNED?

In a finetuned ViT, the feature vector \mathbf{h} has not fully collapsed. It contains a task-relevant component (\mathbf{h}_{task}) that drives the logits \mathbf{g} , and a large residual component ($\mathbf{h}_{residual}$) inherited from ImageNet pretraining that lies in the null space of the finetuning task: $\mathbf{h} = \mathbf{h}_{task} + \mathbf{h}_{residual}$. Since $\mathbf{h}_{residual}$ is orthogonal to the task weights \mathbf{W}_{task} , it does not affect the final prediction \hat{y} for ID samples. However, it does affect the feature norm since $\|\mathbf{h}\|_2 = \sqrt{\|\mathbf{h}_{task}\|^2 + \|\mathbf{h}_{residual}\|^2}$ and the peakedness of the predictive distribution where $\mathbf{h}_{residual}$ often dominates for OOD samples. After global projection filtering, the influence of the subspaces that are more related to the task is preserved, while the subspaces that are not that relevant get discarded in the reconstruction $\mathbf{P}\mathbf{P}^\top \mathbf{h}_{residual} \approx 0$. While this process does not improve the NC geometric properties compared to their NC geometric properties that are computed when no filtering is applied, the probability outputs will get more confident for the classes in the finetuning data, and in turn the probabilistic output will be better suited to detect misclassified inputs.

D.2.2. WHY DOES GRADNORM GLOBAL AND GRADNORM CLASS PRED PERFORM MUCH BETTER THAN VANILLA GRADNORM IN THIS WHEN EVALUATING NEAR, MID, AND FAR OOD FOR ViT MODELS THAT WERE PRETRAINED AND FINETUNED?

Vanilla GradNorm calculates the gradient of the KL divergence with respect to the last-layer weights \mathbf{W} : $\text{GradNorm}(\mathbf{x}) = \|\partial_{\mathbf{w}} \text{KL}(\mathbf{u} \parallel p(\mathbf{x}))\|_p = \left\| \frac{1}{C} \sum_{k=1}^C \frac{\partial \mathcal{L}_{\text{CE}}(g(\mathbf{h}), k)}{\partial \mathbf{w}} \right\|_p$, typically using the L_1 norm. This expression can be factorized into a feature magnitude term $U = \|\mathbf{h}\|_1$ and an output-gradient term $V = \sum_{j=1}^C |1 - C \cdot \mathbf{p}_j|$, which is the sum of absolute differences between class probabilities and the uniform target.

As described previously, in a finetuned ViT, the raw feature \mathbf{h} contains high-variance pretraining residuals inherited from ImageNet, which act as stochastic perturbations in the logit space. These residuals can move an ID sample closer to class boundaries or dilute the activation of the target class, spreading the softmax probabilities \mathbf{p}_j and artificially lowering the output component V at the same time the residual component artificially inflates the feature magnitude term U . By projecting features onto the principal subspace \mathbf{P} , global projection filtering aggressively prunes these irrelevant directions that do not support class-consistent structure. The filtered logit $\hat{\mathbf{g}}$ results in a higher dynamic range between the target class and off-target classes for ID samples, naturally amplifying the peakedness of the predictive distribution and increasing the discriminative score V . Conversely, for OOD samples, the projection $\mathbf{P}\mathbf{P}^\top$ discard the majority of their characteristic pretraining energy, forcing the feature toward the origin after centering. When projected, an OOD sample loses the spurious confidence provided by pretraining features, leading to a flatter, more uniform logit distribution $\hat{\mathbf{g}}$ where $\hat{\mathbf{p}}_j \approx 1/C$. This causes the output component V to collapse toward zero, significantly expanding the safety gap between ID and OOD samples. Thus, projection filtering improves GradNorm by ensuring the output gradient is a true measure of semantic class sensitivity relative to relevant decision boundaries, rather than a noisy response to pretraining variance.

While Global projection filtering removes the residuals, it might still retain the variance of all classes in the task. If classes are crowded (e.g., 100 classes in CIFAR-100), the global subspace \mathbf{P} is still quite large (high rank), allowing an OOD sample to retain significant magnitude by aligning with the principal components of incorrect classes. Class-Predicted Projection

solves this by projecting the feature \mathbf{h} onto the specific subspace $\mathbf{P}_{\hat{y}}$ of the predicted class \hat{y} : $\hat{\mathbf{h}}_{\hat{y}} = \mathbf{P}_{\hat{y}} \mathbf{P}_{\hat{y}}^\top (\mathbf{h} - \boldsymbol{\mu}_{\hat{y}}) + \boldsymbol{\mu}_{\hat{y}}$. This operation is much more aggressive. It discards not only the pretraining noise (null space) but also the variance directions associated with all $K - 1$ other classes. For an ID sample correctly predicted as class \hat{y} , this preserves the signal perfectly because the sample lies in that specific subspace. However, for an OOD sample (or a confused sample) that aligned weakly with \hat{y} only by chance, projecting it onto this narrow, class-specific manifold destroys its magnitude almost entirely.

D.2.3. WHY DOES KPCA GLOBAL AND KPCA CLASS PRED ARE ALSO COMPETITIVE METHODS WHEN EVALUATING NEAR, MID, AND FAR OOD FOR ViT MODELS THAT WERE PRETRAINED AND FINETUNED?

Kernel PCA (KPCA) excels at OOD detection for finetuned ViTs because it replaces the rigid linear assumptions of Neural Collapse with a flexible manifold matching approach. Standard detectors like CTM or fDBD assume that In-Distribution (ID) features collapse into simple, linearly separable clusters (Simplex ETF). However, finetuned ViTs retain a rich, complex geometry from pretraining that violates these assumptions. KPCA addresses this by mapping input features \mathbf{h} into a high-dimensional Reproducing Kernel Hilbert Space via $\psi(\mathbf{h})$ and identifying the principal subspace V that captures the intrinsic non-linear structure of the ID data. The detection metric is the reconstruction error, $e(\mathbf{x}) = \|\psi(\mathbf{h}) - \mathcal{P}_V \psi(\mathbf{h})\|^2$, which quantifies how well a test sample fits this learned manifold rather than measuring its distance to a potentially misaligned centroid.

Crucially, KPCA employs a Cosine-Gaussian kernel to handle the specific geometric irregularities of finetuned representations. This kernel is defined as $k(\mathbf{x}, \mathbf{x}') = \exp\left(-\frac{1}{2\sigma^2} \left\| \frac{\mathbf{h}}{\|\mathbf{h}\|_2} - \frac{\mathbf{h}'}{\|\mathbf{h}'\|_2} \right\|_2^2\right)$, neutralizes the magnitude variance common in finetuned models, ensuring the detector focuses purely on angular alignment. Simultaneously, the Gaussian component models local Euclidean distances on the hypersphere, allowing the subspace to wrap tightly around non-linear, sharpened decision boundaries. This enables KPCA to enclose complex class shapes that linear methods—which effectively fit a flat plane—would fail to capture, thereby reducing false positives from nearby OOD samples.

KPCA is distribution-agnostic regarding this global arrangement; it does not assume a specific prototype location ($\boldsymbol{\mu}_c$) but instead learns the aggregate manifold of all ID data. An OOD sample is detected not because it fails a specific angle test, but because its feature vector contains variance components from the pretraining distribution that are orthogonal to the finetuned task manifold. This ensures that OOD samples yield high reconstruction errors regardless of the symmetry or regularity of the ID class clusters. Similar to GradNorm class pred, KPCA class pred shows an improved performance because the class-predicted projection discards all variance components orthogonal to the predicted class \hat{y} , including generic image statistics and features from competing classes.

E. Hyperparameter selection

All hyperparameters associated to the OOD detection methods are finetuned such that the AUGRC metric is optimized in the validation set. Temperature scaling is tuned on the validation set and applied to all OOD detection methods that used logits as inputs. For Deep Gamblers, the reward is also selected on the validation set.

Table 8. Convolutional Neural Networks.

(a) CIFAR-10

Variation	confidnet					devries					dg				
	base	class	class	class	global	base	class	class	class	global	base	class	class	class	global
avg	pred	avg	pred	avg	pred	avg	pred	avg	pred	avg	pred	avg	pred	avg	pred
Method															
CTM	0	0	0	0	0	0	0	0	0	0	0	0	0	0	0
CTMmean	1	1	0	1	0	0	0	0	0	0	0	0	0	0	0
CTMmeanOC	1	N/A	N/A	N/A	N/A	0	N/A	N/A	N/A	N/A	0	N/A	N/A	N/A	N/A
Confidence	1	N/A	N/A	N/A	N/A	0	N/A	N/A	N/A	N/A	0	N/A	N/A	N/A	N/A
Energy	1	1	1	1	1	1	1	0	1	1	1	1	0	1	1
GE	1	1	0	1	1	1	1	0	1	1	0	0	0	1	0
GEN	0	1	0	1	0	0	0	0	0	0	0	0	0	0	0
GradNorm	1	N/A	1	1	1	1	N/A	1	1	1	1	N/A	1	1	1
KPCA RecError	N/A	0	1	1	1	N/A	0	1	0	0	N/A	0	1	0	0
MLS	1	1	1	1	1	1	1	0	1	1	1	1	0	1	1
MSR	1	1	0	1	1	0	0	0	0	0	0	0	0	0	0
Maha	1	N/A	0	0	0	0	N/A	0	0	0	0	N/A	0	0	0
NNGuide	1	N/A	1	1	1	1	N/A	1	1	1	1	N/A	0	1	1
NeCo	1	N/A	N/A	N/A	N/A	1	N/A	N/A	N/A	N/A	1	N/A	N/A	N/A	N/A
PCA RecError	N/A	0	0	0	1	N/A	0	1	0	1	N/A	0	0	0	1
PCE	1	1	0	1	1	0	0	0	0	0	0	0	0	0	0
PE	1	1	0	1	1	0	0	0	1	0	0	0	0	0	0
REN	0	0	0	0	0	0	0	0	0	0	0	0	0	0	0
Residual	1	N/A	N/A	N/A	N/A	1	N/A	N/A	N/A	N/A	1	N/A	N/A	N/A	N/A
ViM	1	N/A	N/A	N/A	N/A	1	N/A	N/A	N/A	N/A	0	N/A	N/A	N/A	N/A
fDBD	0	N/A	0	0	0	0	N/A	0	0	0	0	N/A	0	0	0
pNML	0	N/A	1	0	0	1	N/A	0	0	1	0	N/A	1	0	0

(b) SuperCIFAR-100

Variation	confidnet					devries					dg				
	base	class	class	class	global	base	class	class	class	global	base	class	class	class	global
avg	pred	avg	pred	avg	pred	avg	pred	avg	pred	avg	pred	avg	pred	avg	pred
Method															
CTM	0	0	0	0	0	0	0	0	0	0	0	0	0	0	0
CTMmean	0	0	0	0	0	0	0	0	0	0	0	0	0	0	0
CTMmeanOC	0	N/A	N/A	N/A	N/A	0	N/A	N/A	N/A	N/A	0	N/A	N/A	N/A	N/A
Confidence	0	N/A	N/A	N/A	N/A	0	N/A	N/A	N/A	N/A	0	N/A	N/A	N/A	N/A
Energy	1	1	0	1	1	1	1	0	1	1	1	1	1	1	1
GE	0	0	0	1	0	1	1	0	1	1	1	1	1	1	1
GEN	0	0	0	0	0	0	0	0	0	0	0	0	0	1	0
GradNorm	1	N/A	1	1	1	1	N/A	1	1	1	1	N/A	1	1	1
KPCA RecError	N/A	0	1	0	0	N/A	0	1	0	0	N/A	0	1	0	0
MLS	0	0	0	0	0	1	1	0	1	1	1	1	1	1	1
MSR	0	0	0	0	0	0	0	0	1	0	1	0	0	1	1
Maha	1	N/A	0	0	0	1	N/A	0	0	0	0	N/A	0	0	0
NNGuide	0	N/A	0	0	0	0	N/A	0	0	0	0	1	1	1	1
NeCo	0	N/A	N/A	N/A	N/A	1	N/A	N/A	N/A	N/A	1	N/A	N/A	N/A	N/A
PCA RecError	N/A	0	0	0	1	N/A	0	1	0	1	N/A	0	1	0	1
PCE	0	0	0	0	0	0	0	0	1	0	1	0	0	1	1
PE	0	0	0	0	0	1	0	0	1	0	1	1	0	1	1
REN	0	0	0	0	0	0	0	0	0	0	0	0	0	0	0
Residual	1	N/A	N/A	N/A	N/A	1	N/A	N/A	N/A	N/A	0	N/A	N/A	N/A	N/A
ViM	0	N/A	N/A	N/A	N/A	0	N/A	N/A	N/A	N/A	0	N/A	N/A	N/A	N/A
fDBD	0	N/A	0	0	0	0	N/A	0	0	0	0	N/A	0	0	0
pNML	1	N/A	0	0	0	1	N/A	1	0	1	0	N/A	1	0	0

(c) CIFAR-100

Variation	confidnet					devries					dg				
	base	class	class	class	global	base	class	class	class	global	base	class	class	class	global
Method	avg	pred	avg	pred	avg	pred	avg	pred	avg	pred	avg	pred	avg	pred	avg
CTM	0	0	0	0	0	0	0	0	0	0	0	0	0	0	0
CTMmean	1	1	1	1	1	0	0	0	0	0	0	0	0	0	0
CTMmeanOC	1	N/A	N/A	N/A	N/A	0	N/A	N/A	N/A	N/A	0	N/A	N/A	N/A	N/A
Confidence	1	N/A	N/A	N/A	N/A	0	N/A	N/A	N/A	N/A	0	N/A	N/A	N/A	N/A
Energy	1	1	1	1	1	0	0	0	0	0	0	0	0	0	0
GE	1	1	1	1	1	0	0	0	0	0	0	0	0	0	0
GEN	0	0	0	0	0	0	0	0	0	0	0	0	0	0	0
GradNorm	1	N/A	1	1	1	1	N/A	1	1	1	1	N/A	1	1	1
KPCA RecError	N/A	0	1	0	1	N/A	0	1	0	0	N/A	0	0	0	0
MLS	1	1	1	1	1	0	0	0	0	0	0	0	0	0	0
MSR	0	0	0	0	0	0	0	0	0	0	0	0	0	0	0
Maha	0	N/A	0	0	0	0	N/A	0	0	0	0	N/A	0	0	0
NNGuide	1	N/A	1	1	1	0	N/A	1	0	0	0	N/A	0	0	0
NeCo	1	N/A	N/A	N/A	N/A	0	N/A	N/A	N/A	N/A	0	N/A	N/A	N/A	N/A
PCA RecError	N/A	1	0	1	1	N/A	0	1	0	1	N/A	0	0	0	1
PCE	0	0	0	0	0	0	0	0	0	0	0	0	0	0	0
PE	0	0	0	0	0	0	0	0	0	0	0	0	0	0	0
REN	0	0	0	0	0	0	0	0	0	0	0	0	0	0	0
Residual	0	N/A	N/A	N/A	N/A	0	N/A	N/A	N/A	N/A	0	N/A	N/A	N/A	N/A
ViM	0	N/A	N/A	N/A	N/A	0	N/A	N/A	N/A	N/A	0	N/A	N/A	N/A	N/A
fDBD	0	N/A	0	0	0	0	N/A	0	0	0	0	N/A	0	0	0
pNML	1	N/A	0	1	0	1	N/A	0	0	0	1	N/A	0	0	0

(d) TinyImageNet

Variation	confidnet					devries					dg				
	base	class	class	class	global	base	class	class	class	global	base	class	class	class	global
Method	avg	pred	avg	pred	avg	pred	avg	pred	avg	pred	avg	pred	avg	pred	avg
CTM	0	0	0	0	0	0	0	0	0	0	0	0	0	0	0
CTMmean	0	0	0	0	0	0	0	0	0	0	0	0	0	0	0
CTMmeanOC	0	N/A	N/A	N/A	N/A	0	N/A	N/A	N/A	N/A	0	N/A	N/A	N/A	N/A
Confidence	0	N/A	N/A	N/A	N/A	1	N/A	N/A	N/A	N/A	0	N/A	N/A	N/A	N/A
Energy	0	0	0	0	0	0	0	0	0	0	0	0	0	0	0
GE	0	0	0	0	0	0	0	0	0	0	0	0	0	0	0
GEN	0	0	0	0	0	0	0	0	0	0	0	0	0	0	0
GradNorm	0	N/A	0	0	0	0	N/A	0	0	0	0	N/A	0	0	0
KPCA RecError	N/A	0	1	0	0	N/A	0	1	0	0	N/A	0	0	0	0
MLS	0	0	0	0	0	0	0	0	0	0	0	0	0	0	0
MSR	0	0	0	0	0	0	0	0	0	0	0	0	0	0	0
Maha	1	N/A	0	0	0	0	N/A	0	0	0	0	N/A	0	0	0
NNGuide	0	N/A	0	0	0	0	N/A	0	0	0	0	N/A	0	0	0
NeCo	0	N/A	N/A	N/A	N/A	0	N/A	N/A	N/A	N/A	0	N/A	N/A	N/A	N/A
PCA RecError	N/A	0	1	0	0	N/A	0	1	0	0	N/A	0	0	0	0
PCE	0	0	0	0	0	0	0	0	0	0	0	0	0	0	0
PE	0	0	0	0	0	0	0	0	0	0	0	0	0	0	0
REN	0	0	0	0	0	0	0	0	0	0	0	0	0	0	0
Residual	1	N/A	N/A	N/A	N/A	1	N/A	N/A	N/A	N/A	1	N/A	N/A	N/A	N/A
ViM	0	N/A	N/A	N/A	N/A	1	N/A	N/A	N/A	N/A	1	N/A	N/A	N/A	N/A
fDBD	0	N/A	0	0	0	0	N/A	0	0	0	0	N/A	0	0	0
pNML	0	N/A	1	0	1	0	N/A	1	0	1	0	N/A	0	0	0

variation	method	cifar10				superifar100				cifar100				tiny-imagenet-200			
		(none)	class	class	global	(none)	class	class	global	(none)	class	class	global	(none)	class	class	global
		avg	pred			avg	pred			avg	pred			avg	pred		
CTM	1	1	1	1	0	0	0	0	1	1	1	1	0	0	0	0	0
CTMmean	1	1	1	1	0	0	0	0	1	1	1	1	0	0	0	0	0
CTMmeanOC	1	nan	nan	nan	0	nan	nan	nan	1	nan	nan	nan	0	nan	nan	nan	nan
Confidence	1	nan	nan	nan	0	nan	nan	nan	1	nan	nan	nan	0	nan	nan	nan	nan
Energy	1	1	1	1	0	0	0	0	1	1	1	1	0	0	0	0	0
GE	1	1	1	1	0	0	0	0	1	1	1	1	0	0	0	0	0
GEN	1	1	1	1	0	0	0	0	1	1	1	1	0	0	0	0	0
GradNorm	1	nan	1	1	0	nan	0	0	1	nan	1	1	0	0	0	0	0
KPCA RecError	nan	1	1	1	0	0	0	0	1	1	1	1	0	0	0	0	0
ML_S	1	1	1	1	0	0	0	0	1	1	1	1	0	0	0	0	0
MSR	1	1	1	1	0	0	0	0	1	1	1	1	0	0	0	0	0
Maha	1	nan	1	1	0	nan	0	0	1	nan	1	1	0	0	0	0	0
NNGuide	1	1	1	1	0	0	0	0	1	1	1	1	0	0	0	0	0
NeCo	1	nan	1	1	0	nan	0	0	1	nan	1	1	0	0	0	0	0
PCA RecError	nan	1	1	1	0	0	0	0	1	0	1	1	0	0	0	0	0
PCE	1	1	1	1	0	0	0	0	1	1	1	1	0	0	0	0	0
PE	1	1	1	1	0	0	0	0	1	1	1	1	0	0	0	0	0
REN	1	1	1	1	0	0	0	0	1	1	1	1	0	0	0	0	0
Residual	1	nan	nan	nan	0	nan	nan	nan	1	nan	nan	nan	0	nan	nan	nan	nan
VIM	1	nan	nan	nan	0	nan	nan	nan	1	nan	nan	nan	0	nan	nan	nan	nan
IDBD	1	nan	1	1	0	nan	0	0	1	nan	1	1	0	nan	1	0	0
pNML	1	1	1	1	0	0	0	0	1	1	1	1	0	0	0	0	0

Table 10. Vision Transformers.

variation	(none)	cifar10				superifar				cifar100				tiny-imagenet-200				
		class	class	global	pred	(none)	class	class	global	(none)	class	class	global	(none)	class	class	global	
method	avg	pred	pred	avg	pred	avg	pred	avg	pred	avg	pred	pred	avg	pred	avg	pred	avg	
CTM	2.2	2.2	10.0	2.2	3.0	10.0	3.0	10.0	3.0	10.0	15.0	10.0	15.0	15.0	15.0	15.0	15.0	
CTMmean	10.0	10.0	10.0	10.0	10.0	10.0	10.0	10.0	10.0	15.0	6.0	10.0	6.0	10.0	15.0	15.0	15.0	
CTMmeanOC	10.0	nan	nan	nan	nan	10.0	nan	nan	nan	6.0	nan	nan	nan	15.0	nan	nan	nan	
Confidence	2.2	nan	nan	nan	3.0	nan	nan	nan	nan	10.0	nan	nan	nan	15.0	nan	nan	nan	
Energy	3.0	3.0	10.0	3.0	3.0	20.0	20.0	20.0	20.0	15.0	15.0	10.0	15.0	15.0	15.0	15.0	15.0	
GE	10.0	10.0	10.0	3.0	10.0	20.0	20.0	20.0	20.0	15.0	15.0	10.0	10.0	15.0	15.0	15.0	15.0	
GEN	10.0	10.0	10.0	10.0	10.0	10.0	10.0	10.0	10.0	20.0	10.0	10.0	10.0	15.0	10.0	10.0	10.0	
GradNorm	3.0	nan	6.0	3.0	3.0	20.0	nan	20.0	20.0	20.0	20.0	20.0	20.0	15.0	nan	10.0	10.0	
KPCA RecError	nan	10.0	6.0	10.0	2.2	nan	10.0	20.0	10.0	nan	15.0	15.0	6.0	nan	15.0	15.0	15.0	
MLS	3.0	3.0	10.0	3.0	3.0	20.0	20.0	20.0	20.0	15.0	15.0	10.0	15.0	15.0	15.0	15.0	15.0	
MSR	10.0	10.0	10.0	10.0	10.0	20.0	10.0	10.0	20.0	15.0	15.0	10.0	10.0	15.0	15.0	10.0	15.0	
Maha	2.2	nan	2.2	2.2	2.2	2.2	nan	2.2	3.0	2.2	6.0	nan	6.0	6.0	6.0	15.0	20.0	15.0
NNGuide	3.0	nan	10.0	3.0	3.0	20.0	nan	20.0	20.0	15.0	nan	10.0	15.0	15.0	15.0	15.0	15.0	
NeCo	3.0	nan	nan	nan	20.0	nan	nan	nan	15.0	nan	nan	nan	15.0	nan	nan	nan	nan	
PCA RecError	nan	10.0	6.0	10.0	10.0	nan	10.0	20.0	10.0	20.0	15.0	10.0	15.0	20.0	nan	15.0	15.0	
PCE	10.0	10.0	10.0	10.0	10.0	20.0	10.0	10.0	20.0	15.0	15.0	10.0	10.0	15.0	15.0	15.0	15.0	
PE	10.0	10.0	10.0	10.0	10.0	20.0	20.0	10.0	20.0	15.0	15.0	10.0	10.0	15.0	15.0	10.0	15.0	
REN	10.0	10.0	10.0	10.0	10.0	10.0	10.0	10.0	10.0	10.0	10.0	10.0	10.0	15.0	15.0	10.0	15.0	
Residual	2.2	nan	nan	nan	2.2	nan	nan	nan	6.0	nan	nan	nan	20.0	nan	nan	nan	nan	
ViM	2.2	nan	nan	nan	2.2	nan	nan	nan	15.0	nan	nan	nan	20.0	nan	nan	nan	nan	
fDBD	2.2	nan	6.0	3.0	2.2	10.0	nan	10.0	10.0	15.0	nan	15.0	15.0	15.0	15.0	15.0	15.0	
pNML	10.0	nan	6.0	10.0	2.2	nan	10.0	10.0	2.2	20.0	nan	10.0	6.0	15.0	15.0	15.0	10.0	